Mid-Infrared Variability in Nearby Galaxies from the MaNGA Sample

AASHAY PAI , MICHAEL R. BLANTON , AND JOHN MOUSTAKAS 2

¹Center for Cosmology and Particle Physics Department of Physics, New York University, 726 Broadway, New York, NY 10003, USA ²Department of Physics and Astronomy, Siena College, 515 Loudon Road, Loudonville, NY 12211, USA

ABSTRACT

We use mid-infrared variability in galaxies to search for active galactic nuclei (AGN) in the local universe. We use a sample of 10,220 galaxies from the Mapping Nearby Galaxies at APO (MaNGA) survey, part of the Sloan Digital Sky Survey (SDSS-IV). For each galaxy, we examine its mid-infrared variability in the W2 [4.6 µm] band over thirteen years using data from the Wide Infrared Survey Explorer (WISE) All-Sky and Near Earth Objects WISE (NEOWISE) missions. We demonstrate that we can detect variability signatures as small as about 7% in the root-mean-square variation of W2 flux for the majority of cases. Using other AGN signatures of the variable galaxies, such as optical narrow lines, optical broad lines, and WISE W1-W2colors, we show that $\sim 75\%$ of the variables show these additional AGN signatures, indicating that the bulk of these cases are likely to be AGN. We also identify seven galaxies that have light-curves characteristic of tidal disruption events. We present here a publicly available catalog of the light-curve variability in W2 of these galaxies.

Keywords: Active Galactic Nuclei, MaNGA, WISE

1. INTRODUCTION

Active Galactic Nuclei (AGN) are accreting supermassive black holes at the centers of galaxies, whose radiation across the electromagnetic spectrum is powered by energy released as matter descends into the black holes' potential wells.

Emission from the AGN accretion disk, where most of this energy release occurs, heats the gas and dust surrounding it. Many AGN are surrounded by a dusty structure, with a size scale of order $1-10\,\mathrm{pc}$, referred to as the "dust torus" (Hickox & Alexander 2018). The inner parts of this torus reach up to about 1500 K, corresponding to the dust sublimation temperature (at smaller radii from the black hole, the dust is therefore destroyed). These inner regions are responsible for thermal dust emission peaking around 2-4 µm (Lyu & Rieke 2022), with the outer, cooler regions contributing emission out to 40 µm.

typically lies a broad line region (BLR), characterized by high gas velocities (1,000s of km s⁻¹) within the gravitational sphere of influence of the

Closer to the accretion disk than the dusty torus

black hole. Galaxies with observed broad emission lines are classified as Seyfert Type 1. However, the BLR can be obscured by the dusty torus and in such cases is unobservable except as polarized scattered light (Antonucci 1983). These AGN are typically still observable from emission lines emanating from the Narrow Line Region, which extends to 100s of pc and sometimes several kpc (Hickox & Alexander 2018). These AGN are classified as Seyfert Type 2.

Their mid-IR emission make AGN spectra stand out from purely star-forming galaxies. The former have narrow emission lines interspersed between a smooth continuum, whereas the latter show prominent Polycyclic Aromatic Hydrocarbon (PAH; Smith et al. 2007) lines and substantially cooler thermal dust emission instead. This difference makes the Wide Infrared Survey Explorer (WISE; introduced in Section 2.1.2) a natural candidate to be used for identifying AGN. Stern et al. (2012) introduced criteria in WISE W1 and W2 fluxes to detect a mix of Type 1 and Type 2 AGN.

As an illustration, Figure 1 shows Spectral Energy Distribution (SED) fits to galaxy broad band photometry for three MaNGA galaxies. These fits are to ultraviolet far- and near-ultraviolet bands from the Galaxy Evolution Explorer (GALEX; Morrissey et al. 2007), the DESI Legacy Imaging Surveys (LS; Dey et al. 2019), and WISE photometry. The model contains two different contributions, fit simultaneously. The first is a stellar population synthesis fit, using a nonnegative linear combination of a broad range of templates from the Flexible Stellar Population Synthesis code (FSPS; Conroy & Gunn 2010); these templates include dust attenuation and reemission. The second uses templates from the AGN, using the CLUMPY models of Nenkova et al. (2008). The black line is the total SED, and the green is the AGN contribution.

Each spectrum represents a different type of galaxy—quiescent, star-forming or AGN. The WISE bands are labeled in the mid-infrared wavelengths. Panel (a) shows a quiescent galaxy with a steep, very blue mid-infrared spectrum dominated by the Rayleigh-Jeans tails of the stellar emission. Galaxies like this one have correspondingly low W3 and W4 fluxes, because they do not contain large amounts of warm dust, the main contributor to this emission. Panel (b) shows a starforming galaxy, with high W3 and W4 due to the presence of the warm dust and PAHs associated with star formation The ratio of W1 to W2 fluxes for both quiescent and star-forming galaxies are largely unperturbed by the warm dust and PAHs, and these galaxies typically have bluer W1 - W2colors. Panel (c) shows a galaxy with an AGN in which the SMBH heats the dust to sublimation temperatures, causing an increase in the W2 emission from this hot dust, thereby changing the W1 to W2 ratio, and causing a redder W1 - W2 color.

In this paper we seek to identify variable AGN. Whereas longer IR wavelengths are less prone to variation, near IR wavelengths around 1–5 µm vary on human timescales, because this emission is caused by the dust reverberation response due to variations in the accretion disk, as confirmed by the time lag between observed IR and UV fluxes (Lyu & Rieke 2022). Based on the above discussion of Figure 1, the variability in the amplitude of the AGN will be fractionally larger in W2 than W1. For many star forming galaxies the fractional W2 variation will also exceed W3 or W4. Since WISE observed in W1 and W2 longer than W3 and W4, we will concentrate on the variability of W2 here.

With these motivations in mind, we create a WISE catalog using the MaNGA sample (introduced in Section 2.1.1), by analyzing the variability of the WISE All-Sky and NEOWISE observations of these galaxies. We further define a

new variability criterion to identify AGN in the MaNGA sample. In Section 2.1 we give descriptions of MaNGA and WISE. In Section 2.2 we give a broad overview of our methodology to determine variability, in Section 2.3 we describe the calculations performed to determine variability and the contents of the catalog, in Section 2.4 we define what objects we consider to be variable, and in Section 2.5 we verify our variable sample by looking at their optical narrow line, optical broad line and W1 - W2 colors. We show MaNGA images and spectra of a few variable galaxies in Section 3. Section 4 summarizes our work and Section 5 explains how the catalog can be accessed.

All magnitudes are on the AB system (Oke & Schild 1970) throughout. We have converted the Vega-relative magnitudes published by WISE using the kcorrect 5.1.2 Python package (Blanton & Roweis 2007).

2. METHODS

2.1. Galaxy Selection

The galaxies in this catalog are selected from the Mapping Nearby Galaxies at APO (MaNGA; Bundy et al. 2014) component of the Sloan Digital Sky Survey IV (SDSS-IV; Blanton et al. 2017). We match these galaxies to the Wide Infrared Survey Explorer's (WISE; Wright et al. 2010) WISE All-Sky and Near Earth Objects WISE (NEOWISE; Mainzer et al. 2014) missions.

2.1.1. MaNGA Overview

MaNGA is an integral field survey that observed 11,273 objects using the Sloan Foundation Telescope at Apache Point Observatory, New Mexico as part of SDSS-IV. It used the Baryon Oscillation Spectroscopic Survey (BOSS) spectrographs connected to 17 optical fiber bundles (Drory et al. 2015; Smee et al. 2013).

The sample contains all types of nearby galaxies ($z \le 0.15$) with stellar masses between 10^9 to $10^{11}~M_{\odot}$, divided into Primary, Secondary, and Color-Enhanced samples. Using these observations, the Data Reduction Pipeline built data cubes by extracting spectra from the fibers (Law et al. 2015, 2016). The Data Analysis Pipeline then further processed the data to extract velocity dispersion and emission line flux measurements (Westfall et al. 2019).

Sánchez et al. (2022) analyzed the MaNGA datacubes using the pyPipe3D data pipeline, to produce the Pipe3D Value Added Catalog, which we use here. This catalog contains various measure-

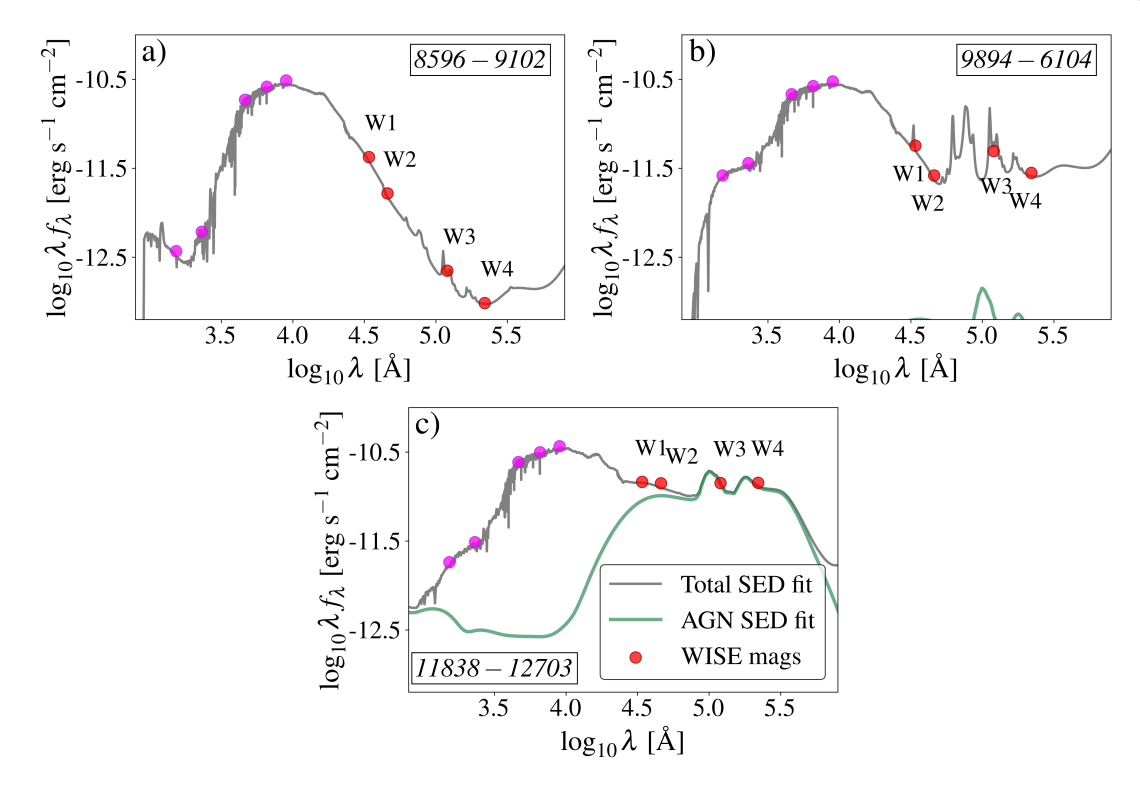


Figure 1. MaNGA SED fits on (a) quiescent, (b) star-forming, and (c) AGN galaxies. The grey lines are the total SED fit to broad band photometry, the green lines are the estimated AGN component. The fuchsia points are the GALEX NUV & FUV and the LS grz bands (from left to right). The red points are the four WISE magnitudes - W1, W2, W3 and W4. Each panel is labelled by its MaNGA identifier plate-IFU. Only the galaxy dominated by the AGN component in mid-IR demonstrates an increase in W2 flux, therefore contributing to a redder W1 - W2 color.

ments regarding the stellar populations, star formation histories, emission lines, and other properties of galaxies.

We create and analyze images for GALEX farand near-ultraviolet, LS grz, and WISE bands. We calculate elliptical aperture photometry for all MaNGA galaxies, which we use here for midinfrared W1 - W2 color measurements.

2.1.2. WISE Overview

WISE is a NASA Explorer launched in 2009 and put into hibernation in 2011. WISE collected data using a 40-cm cryogenically-cooled telescope which contained four mid-infrared detectors and imaged the entire sky in band passes at 3.4, 4.6, 12, and $22 \mu m$, referred to as W1, W2, W3, and W4. These band passes have a resolution of 6.1'', 6.4'', 6.5'', and 12.0'' (Wright et al. 2010).

The WISE All-Sky survey contains data collected during the full cryogenic mission phase, which took place from January 2010 through August 2010. The processed catalog contained photometric observations of over 563 million detected objects.

WISE was brought out of hibernation in 2013 for the NEOWISE mission (Mainzer et al. 2014). The WISE Moving Object Pipeline System searches for near-Earth objects, comets, and small planets. The NEOWISE mission also processes observations of other WISE objects through the standard WISE pipeline used for the All-Sky survey.

2.2. Overview of Methodology

We calculate W2 variability because, as explained above, it is a good indicator of AGN activity. To do so, we search for objects with a variance in their observed fluxes that exceed the variance expected from observational uncertainties. We use the individual WISE All-sky and NEOWISE W2 observations binned into "epochs," which WISE observed on a six-month cadence. We then use these W2 light-curves to calculate the observed variance across all epochs of the mean magnitudes per epoch (Equation 8). We compare this quantity to the variance in the mean magnitude per epoch expected from an empirical estimate of the observational uncertainties (Equation 10). This procedure estimates the W2 variability relative to expectations. To determine which objects are reliably classifiable as variable, we perform a Monte Carlo simulation to identify how much larger than expectations the variance must be to ensure a pure sample of variables. We define objects with higher variability than expected in this sense as "variable in the mid-IR."

2.3. Quantifying W2 Variability

We combine the WISE All-Sky and NEOWISE observations for each object to quantify the variability of these objects between January 2010 and December 2022. We use data from the single source "L1b" tables, specifically the w1mpro and w2mpro columns, which contain magnitudes measured with profile-fitting photometry. ing each epoch of observation, WISE made an average of 15 observations of each object over the span of a day. There are two epochs during each year for which WISE was active. We query the WISE database with a tolerance of 2 arcseconds in right ascension and declination, and then further filter out all matches that have uncertainties in RA and Dec of more than 1 arcsecond. We also require that the overall frameset quality score flag (qual_frame)—which can be 0, 5 or 10, with 10 being the best quality—be nonzero. Finally, we filter out all observations that have been flagged with a contamination and confusion flag (cc_flags), which identifies diffraction spikes, persistence, anneal-resistant latent images, halos, optical ghosts, long-term latent images and glints. We only use galaxies that have detections in 4 or more epochs (using epoch_flag, see Table 2).

We calculate the following statistical quantities to determine the variability of the galaxies in the sample. All quantities are calculated using the observations stored in the w1mpro and w2mpro columns and the estimated errors in the w2sigmpro and w2sigmpro columns. In the notation below, *j* indexes each epoch and *i* indexes each observation within an epoch.

- Number of good observations at each epoch n_i.
- Number of epochs per object N.
- Mean W2 magnitude of each epoch.

$$\overline{W2}_j \equiv \frac{1}{n_j} \sum_{i=1}^{n_j} (W2)_{ij}$$
 (1)

 Expected variance within each epoch (based on catalog errors): expected variance in the magnitudes within each epoch estimated from the reported catalog uncertainties.

$$\sigma_{\text{ep},j}^2 \equiv \frac{1}{n_i} \sum_{i=1}^{n_j} \sigma_{ij}^2$$
 (2)

• Observed variance within each epoch (based on within-epoch magnitudes): variance in the observed W2 magnitudes per epoch.

$$Var(W2_{ep,j}) \equiv \frac{1}{n_j - 1} \sum_{i=1}^{n_j} (W2_{ij} - \overline{W2}_j)^2$$
(3)

• Expected variance in the mean within each epoch (based on catalog errors).

$$\sigma_j^2 \equiv \frac{\sigma_{\text{ep},j}^2}{n_j} \tag{4}$$

• Expected variance in the mean within each epoch (based on within-epoch magnitudes):

$$\varsigma_j^2 \equiv \frac{\text{Var}(W2_{\text{ep},j})}{n_j} \tag{5}$$

• Error in mean per epoch (using the quantity defined in Equation 5).

$$\sigma_{\overline{\text{W2}},j} \equiv \varsigma_j$$
 (6)

• Observed variance across all epochs: the variance of the mean *W*2 magnitudes of each epoch (Equation 8). First, we define the mean of the magnitude over all epochs:

$$\mu(\overline{W2}) \equiv \sum_{i=1}^{N} \frac{\overline{W2}_{j}}{N} \tag{7}$$

and we use it to calculate the observed variance:

$$Var(W2) \equiv \frac{\sum_{j=1}^{N} \left(\overline{W2}_{j} - \mu(\overline{W2}) \right)^{2}}{N-1}$$
 (8)

 Expected variance across all epochs (based on catalog sigma): the epoch-to-epoch variance in the mean magnitude calculated using the estimated errors

$$\sigma^2 \equiv \sum_{i=1}^N \frac{\sigma_j^2}{N} \tag{9}$$

 Expected variance across all epochs (based on within-epoch variances): the epoch-toepoch variance in the mean magnitude calculated using the per epoch variance in the observed magnitude,

$$\varsigma^2 \equiv \sum_{i=1}^N \frac{\varsigma_j^2}{N} \tag{10}$$

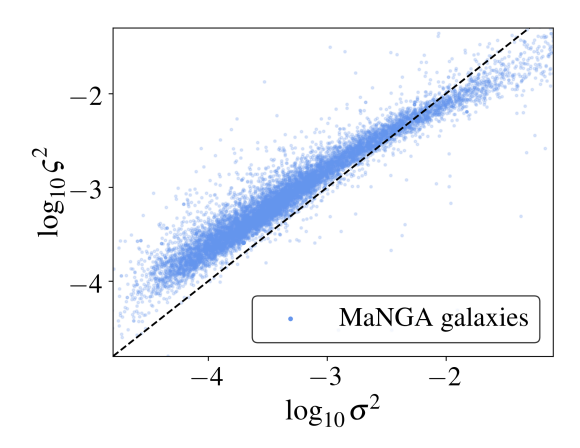


Figure 2. Comparing the expected variance derived from within-epoch variances (Equation 10) to the expected variance derived from within-epoch uncertainties (Equation 9). 81% of the MaNGA sample lies above the one-to-one line ($\zeta^2 > \sigma^2$). We therefore conservatively use ζ^2 as our true errors.

Figure 2 compares the expected variance across all epochs derived from within-epoch variances (ζ^2 in Equation 10) to the expected variance across all epochs derived from reported catalog uncertainties (σ^2 in Equation 9). There is substantial disagreement between these estimates, and for around 81% of our galaxies, σ^2 is much larger.

We do not expect that these galaxies show substantial variability on hour or day long time scales. In any case, to explain the difference, the variability would have to correlate well with the expected uncertainties, which seems implausible. Therefore this result appears to show that the reported uncertainties are unreliable and do not reflect the true uncertainties. Therefore, we use Equation 10 instead of Equation 9 for our analysis in the subsequent sections.

2.4. Identifying Variable Sources

We determined the variability of the MaNGA galaxies using the epoch-to-epoch variability calculations performed in Sec. 2.3. Figure 3 compares the observed variance across all epochs (Equation 8) versus the expected variance across all epochs based on within-epoch variances (Equation 10). Most of the galaxies show a one-toone correspondence between the observed and expected variances, and we classify these galaxies as non-variable. They show slightly higher observed variance then expected, which is presumably due to systematic errors arising between epochs that are not captured in the within-epoch variance. This additional variance appears to become a little stronger at higher expected variance values (in the upper right) and at the lowest expected variances (the "floor" in the the observed variance below $\log_{10} \zeta^2 \sim -3.0$). The floor presumably arises due to calibration-related systematics across epochs.

Galaxies in the top-left of this diagram exhibit variability over epochs that is much higher than that which is expected of them due to noise, and we classify these objects as variable in the mid-IR. We have a choice in how we design our classification scheme; we can set a high threshold for variability, which will be detectable for a larger fraction of the objects, or a lower threshold, which is only detectable for the highest signal-to-noise objects. Figure 3 shows our default choice as the shaded region, which is defined in Equation 11.

$$\log_{10} \text{Var}(W2) > -2.3$$

$$\log_{10} \zeta^2 < -2.5 \qquad (11)$$

$$\log_{10} \text{Var}(W2) > \log_{10} \zeta^2 + 0.7$$

We determined this region by performing a Monte Carlo simulation consisting of 100,000 realizations to estimate the expected distribution of Var(W2) in the hypothetical case that none of the objects are variable. We bin the data by $\log_{10} \zeta^2$, and compute the mean $\log_{10} \text{Var}(W2)$ per bin (which we assume to be the true variance in the measurements of a non-varying object due to observational effects). We then randomly sample a galaxy, find the corresponding mean $log_{10} Var(W2)$ (based on its bin), and assume individual epochs will be distributed as a Gaussian with a variance Var(W2). We sample 25 points from this Gaussian (which is the average number of epochs for all the galaxies) and recompute the $log_{10} Var(W2)$ with this Monte Carlo data.

This procedure results in a distribution of $\log_{10} \text{Var}(W2)$ as a function of $\log_{10} \varsigma^2$. This distribution is actually somewhat tighter around the data's mean in each bin than the data is. We therefore apply a fudge factor of 1.25 to inflate the width of the Monte Carlo distribution around the mean. We set this factor to match the negative tail of the distribution; the origin of this factor is not entirely clear, but it presumably arises from non-Gaussianity in the real errors and the fact that some fraction of galaxies were observed fewer than 25 times.

Fig. 4 shows the distribution of $\log_{10} \text{Var}(W2)$ predicted by the Monte Carlo simulations (including the fudge factor) and the values calculated using WISE data, for the data with $\log_{10} \zeta^2 < -2.5$.

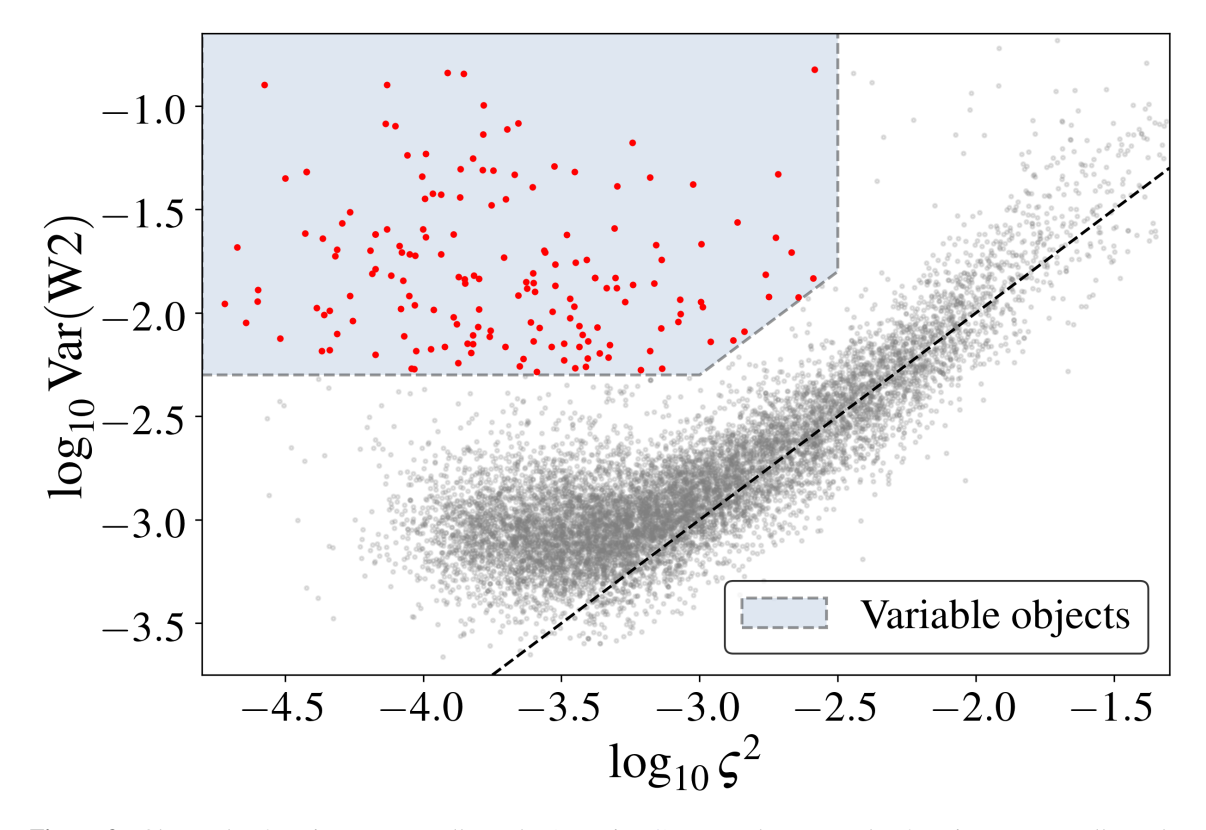


Figure 3. Observed W2 variance across all epochs (Equation 8) versus the expected W2 variance across all epochs calculated from within-epoch variances (Equation 10) for MaNGA galaxies. Galaxies in red are defined to be "variable in the mid-IR" in Sec. 2.4.

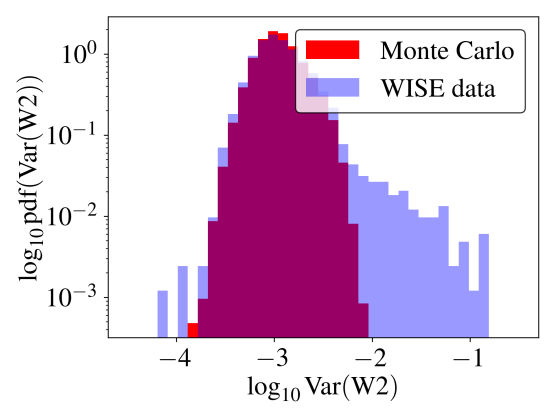


Figure 4. Distribution of predicted points using Monte Carlo simulations vs. the observed $\log_{10} \text{Var}(W2)$, only using points with $\log_{10} \zeta^2 < -2.5$.

The tail at high $\log_{10} \text{Var}(W2)$ contains the identified variable objects.

Our procedure produces a distribution that closely follows the non-variable object distribution seen in Fig. 3. Using a Monte Carlo realization with roughly ten times the number of samples as we have galaxies, we define the shaded region in Fig. 3 conservatively, such that the region contains zero samples from the Monte Carlo simulation.

This definition leads to 170 galaxies that are identified as variable in the mid-IR. These objects are tagged with a variability flag (var_flag). Figure 5 shows examples of W2 light-curves of two galaxies that we classify as variable in the mid-IR (in blue) and two that have comparable ς^2 , but are not identified as variable in the mid-IR (in orange). The individual points are WISE observations binned into epochs, and the lines are Gaussian process fits to those points. The Gaussian process regression was done using the scikit-learn (Pedregosa et al. 2011) Python package using a Matern-3/2 kernel, with a hyperparameter length scale of \sim 15 years. The GP fit has only been used to visualize the data.

We identify 15 galaxies that fall in our variability cut but either have data for only a few epochs or whose changes in magnitude exist only over one epoch, making the variability questionable. We tag these 15 objects with a visual inspection flag (vi_flag, as described in Table 2).

The expected variance ζ^2 is primarily determined by the mean W2 flux. We therefore look for an approximate W2 magnitude above which our variability determination is complete. Panel (a) of Figure 6 shows $\log_{10} \zeta^2$ and W2 for each galaxy. The vertical line at $\log_{10} \zeta^2 = -2.5$ corresponds to the

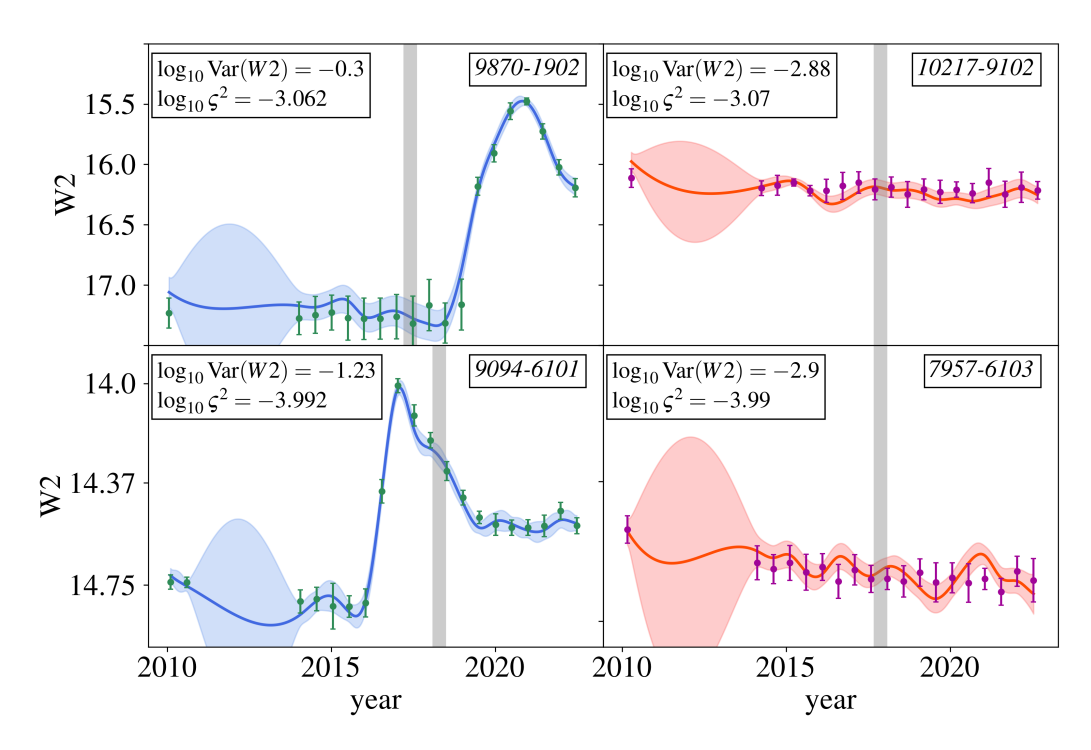


Figure 5. Light-curves of galaxies that are variable in the mid-IR (in blue), and galaxies that are not classified as variable in the mid-IR (in orange). Each panel is labelled by its MaNGA plate-IFU (top right) and its location in our variability space given by $\log_{10} \text{Var}(W2)$ and $\log_{10} \zeta^2$ (top left). The grey band indicates when the object was observed by MaNGA.

vertical boundary of the variable region in Figure 3. The horizontal dashed line is at W2=16.5; around 65% of the galaxies have W2 brighter than 16.5. In this subsample (highlighted in blue), 97% of the galaxies have $\log_{10} \varsigma^2 < -2.5$. Panel (b) of Figure 6 is similar to Figure 3 but only shows the galaxies with W2 < 16.5. We can reliably identify variability greater than $\log_{10} \text{Var}(W2) > -2.3$ if the galaxy has W2 < 16.5, and our catalog is complete subject to these constraints.

2.5. Properties of the Variable Galaxies

In this section, we examine the source of the variability of the galaxies in our catalog by using other well-known methods of identifying AGN. We consider optical narrow and broad lines in MaNGA spectra and the W1-W2 color of these galaxies. We also check if our transients match identified Tidal Disruption Events (TDEs) by looking a three catalogs (Masterson et al. 2024, Wang et al. 2012 & Callow et al. 2024). Finally, we check if our variable objects have matches to Mid-IR Outbursts in Nearby Galaxies (MIRONGs; Jiang et al. 2021) catalog.

Table 1 summarizes the fraction of variable objects that fall into other classification techniques and types of AGN. $N_{\text{var}} = 170$ is the total number

Table 1. Fraction of variable objects from our catalog that are identified as AGN or transients using different classification schemes.

AGN classification scheme	$N/N_{\rm var}$	$N/N_{\rm cat}$
Broad Line AGN (Fu et al. 2023)	0.42	0.39
Narrow Line AGN (Ji & Yan 2020)	0.28	0.12
Red $W1 - W2$ color (Assef et al. 2018)	0.29	0.44
Red $W1 - W2$ color	0.46	0.39
(our modified criterion, see Sec. 2.5.3)		
MIRONGs (Jiang et al. 2021)	0.02	0.03

of variable objects from our catalog. N_{cat} is the number of objects in the catalog being matched to, and N is the number of variable objects from our catalog that are also found in the other catalog.

2.5.1. Broad Line AGN

To examine the overlap between our detected variable galaxies and the detected Type 1 AGN population, we use the catalog from Fu et al. (2023) of broad-line AGN from the MaNGA sample (hereafter called the broad line catalog). Figure 7 shows the distribution of broad line AGN in our variability plot.

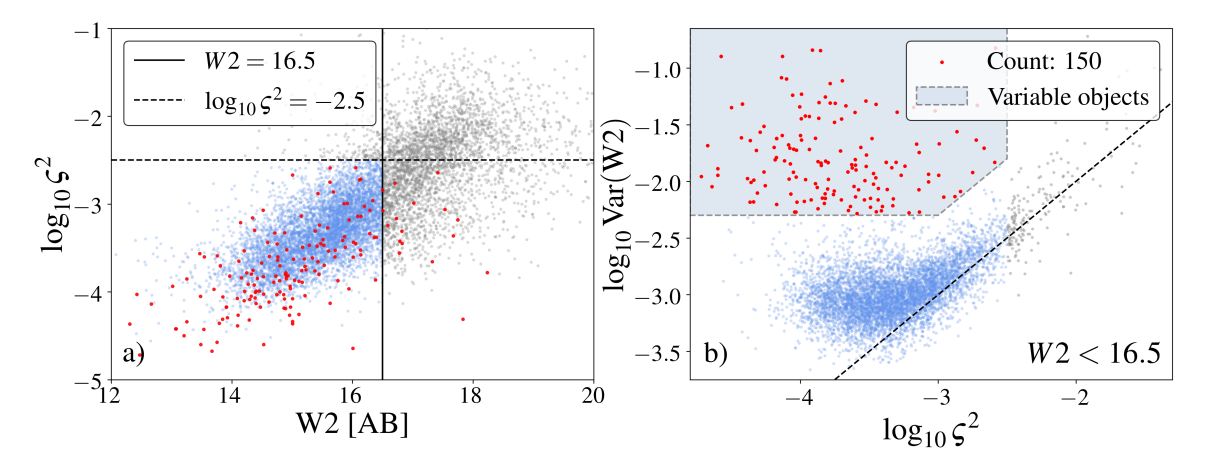


Figure 6. (a) compares $\log_{10} \zeta^2$ vs. W2, with the black line plotting the vertical edge of the variable cut in (b). The galaxies in blue have W2 < 16.5 and $\log_{10} \zeta^2 < -2.5$. (b) show the population with W2 < 16.5. It is also labelled with 'count', which is the number of variable objects that remain after the magnitude cut.

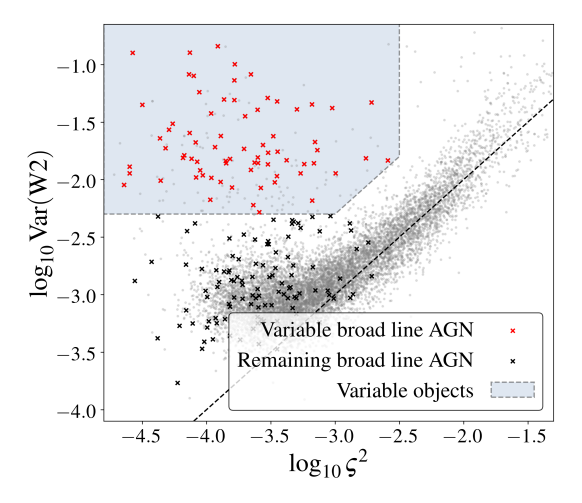


Figure 7. Similar to Figure 3, showing where broad line AGN lie in the space of W2 variability. The grey points are all of the MaNGA galaxies. The red and black crosses are broad line AGN identified in the broad line catalog of Fu et al. (2023). The red crosses are the broad line AGN that we identify as variable in the mid-infrared, and the black are the broad line AGN that we do not identify as variable.

Around 42% of our variable objects have matches in the broad line catalog, and around 39% of the broad line AGN are identified as variable by us. All of the galaxies with broad line AGN have W2 fluxes bright enough that we expect to detect variability with a log variance (in mag² units) greater than about -2.3. This variability limit is relative to the total W2 flux (stellar plus AGN).

2.5.2. Optical Narrow Line AGN

Optical narrow-line diagnostic diagrams are an effective tool for understanding and separating

different ionizing sources in galaxies. Baldwin, Philips, & Terlevich (BPT) diagrams (Baldwin et al. 1981) and Veilleux & Osterbrock (VO) diagrams (Veilleux & Osterbrock 1987) use a combination of [O III]/H β , [N II]/H α and [S II]/H α line ratios (hereafter referred to as R3, N2 and S2) to differentiate between star-forming, AGN host, and low ionization emission region galaxies (LINERs). Specifically, BPT diagrams compare R3 to N2 and VO diagrams compare R3 to S2. Ji & Yan (2020) presents a reprojection of the N2, S2 and R3 line ratio space, claiming that this reprojection, defined in Equation 12, provides a cleaner classification than either BPT or VO individually:

$$P1 = 0.63N2 + 0.51S2 + 0.59R3$$

$$P2 = -0.63N2 + 0.78S2$$

$$P3 = -0.46N2 - 0.37S2 + 0.81R3$$
(12)

Figure 8 shows the distribution of MaNGA galaxies plotted in the narrow line space defined above. We exclude known broad line AGN from this plot using the broad line catalog from 2.5.1, because the DAP measurements of narrow line emission are imperfect in many such cases. We classify galaxies with P1 > -0.3 and P3 > 0.5 as narrow line AGN, and it can be seen that roughly half of the non-broad-line variable objects lie within these bounds. Around 28% of all of the variable objects, and around 49% of the non-broad-line variable objects, are identified as narrow line AGN.

Figure 9 shows the W1 - W2 color of our sample versus $\log_{10} \text{Var}(W2)$, providing an insight into the color distribution of galaxies as a function of

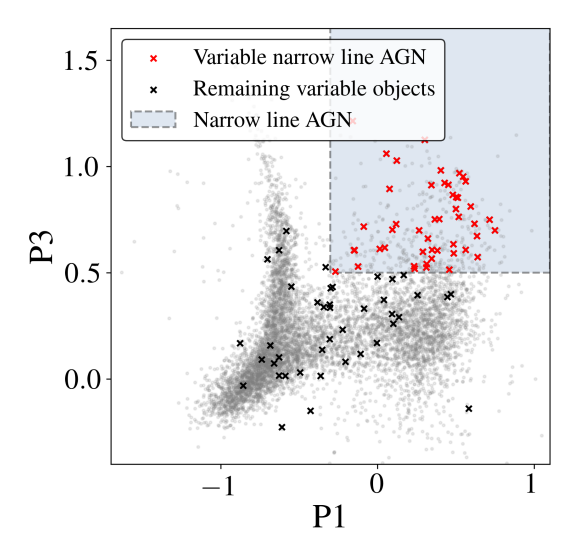


Figure 8. Depicting where our variable galaxies lie in the P1 vs. P3 space, with the grey points being the MaNGA galaxies. The red crosses are variable objects from our catalog that are identified as narrow line AGN based on the criterion from Ji & Yan (2020). The black crosses are the remaining objects that we identify to be variable in the mid-infrared.

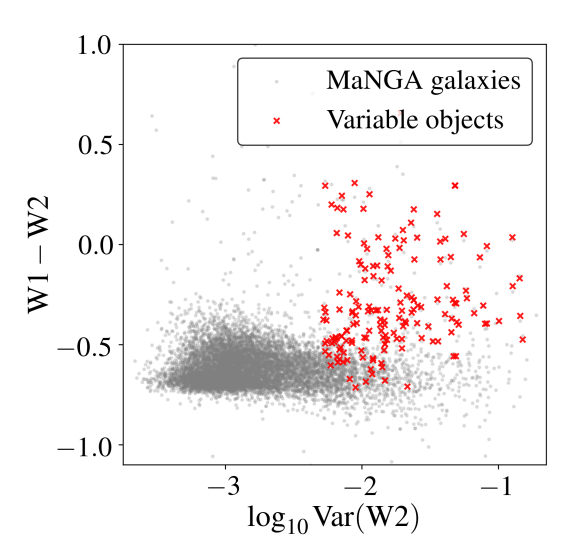


Figure 9. W1 - W2 (AB) colors vs. $\log_{10} Var(W2)$ of our sample. The red points represent our mid-IR variable objects.

their *W*2 variability. Our selection criteria allow objects with high *W*2 variability to be selected irrespective of their non-AGN-like colors. Nevertheless, the identified variable objects tend to have red colors, which indicates that they are mid-IR AGN (Figure 1).

Figure 10 shows the W1 - W2 color of all the MaNGA galaxies as a function of their specific star formation rate (sSFR). the Pipe3D sSFR values are

calculated from the MaNGA aperture. Most galaxies in this plot lie on a tight sequence with blue colors typical of stellar populations, while AGN host galaxies are redder in W1-W2, and therefore skewed upwards (cf. Fig. 1).

Non-AGN galaxies lie well below the cutoff set by Assef et al. (2018), where we use their least conservative (bluest) cutoff, converted to AB magnitudes. Galaxies that we classify as variable are shown in red, and extend into the star-forming sequence below the cutoff.

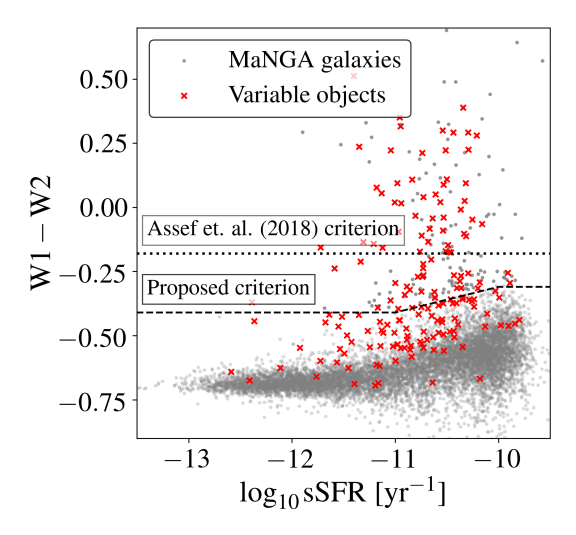


Figure 10. W1 - W2 (AB) colors of MaNGA galaxies vs. their specific star formation rate determined from stellar population analysis. The red points represent our mid-IR variable objects.

We propose a modified color criterion that extends the W1-W2 cutoff closer to the main sequence of star-forming galaxies. Many of the galaxies above this threshold (and some below) are detectably variable, supporting the interpretation of galaxies with these colors as AGN. Overall, the majority of the galaxies selected using our color criteria ($\sim 80\%$) have a match as a broad line, optical narrow line, mid-IR variable, or red W1-W2 (using the Assef et al. 2018 cut) AGN. This criterion therefore allows for a more complete population of AGN in nearby galaxies from their colors, with strong evidence that most if not all of these galaxies host true AGN.

Using the criterion from Assef et al. (2018), about 29% of the galaxies that we classify as variable are mid-IR color selected AGN. Using our modified criterion, around 46% of the variable galaxies are mid-IR color selected AGN.

Jiang et al. (2021) describes a catalog of Mid InfraRed Outbursts in Nearby Galaxies (MIRONGs), which they define as galaxies that display a flare of at least 0.5 mag in the mid-IR preceded by a stable phase without variability. The catalog was created from a sample selected from galaxies in the SDSS DR14 (Abolfathi et al. 2018) by looking at their WISE variability from the NEOWISE database. Although their parent sample has significant overlap with MaNGA, our criterion is much more sensitive which is why only a small fraction of our galaxies appear as Mid-IR outbursts, which are more similar to changing look AGN or TDEs. Around 2% (4 galaxies) of our variable objects have matches to MIRONGs from this catalog.

2.5.5. Tidal Disruption Events

Masterson et al. (2024) identifies 18 Tidal Disruption Events (TDEs) in nearby galaxies ($< 200\,\mathrm{Mpc}$, or z < 0.05) that were found using NE-OWISE data. They look for transients across the NEOWISE database, and then cross-match it with the Census of the Local Universe (CLU; Cook et al. 2019), thus enforcing the 200 Mpc criteria. The population of galaxies that they end up with therefore may not necessarily have a large overlap with the MaNGA sample.

They select events to have light-curves with a stable period before a rapid flare, followed by a slow monotonic decline. They also ensure that the W2 light-curve luminosity is greater than $10^{42}\,\mathrm{erg}\,\mathrm{s}^{-1}$ and that the galaxy has non-AGN WISE colors. We find one match between our mid-IR variable objects and these TDE candidates, which they denote "WTP 16aatsnw" and which corresponds to plate-IFU 11981-6104. They conclude that this galaxy is an AGN based on its location in BPT diagrams made using SDSS archival spectroscopy. However, they note that this object does not have or X-ray emission. As we note below, its W1 - W2 colors are variable, indicative of hot dust during its bright period and consistent with a stellar population otherwise.

Extreme Coronal Line Emitting galaxies are TDEs whose spectra contain very high ionization forbidden spectral lines such as [Fe VII], [Fe X] and [Fe XIV]. Wang et al. (2012) finds seven galaxies from the SDSS DR7 (Abazajian et al. 2009) with z < 0.38 whose spectra show the presence of these coronal lines. Callow et al. (2024) adds seven new candidates to this catalog of ECLEs by searching through the SDSS Legacy DR17 (Abdurro'uf et al. 2022). We look for

matches between our variable galaxies and these 14 ECLEs but do not find any, as these galaxies are not present in the MaNGA sample.

2.5.6. Comments on Properties of Mid-IR Variable Galaxies

The overlap of our variable catalog with AGN samples clearly shows that many of the identified variables are associated with AGN. AGN identified with broad lines, narrow lines, and mid-IR colors are clearly overrepresented in the variable sample. We find that 74% of our mid-IR variable galaxies show one of these additional AGN signatures, using the Assef et al. (2018) criterion for WISE color. This number increases to 80% if we use our WISE color criterion instead.

That said, we caution the reader against inferences about the true AGN population from the numbers in Table 1. The overlap among these samples is affected by selection effects in all of the AGN signifiers, and correct inferences require a much more detailed analysis accounting for such effects. For this purpose, Figure 6 demonstrates that we can can detect variability with $\log_{10} \text{Var}(W2) > -2.3$, for all galaxies brighter than $W2 \sim 16.5$. Even in this case, the relative W2brightness of the AGN relative to the host galaxy needs to be accounted for, as a 7% variation in total flux (as seen in a majority of our mid-IR variable objects) may reflect a much larger variation of the AGN flux. Future work is required to infer the true joint distribution of these AGN manifestations.

3. EXAMPLES OF MID-IR VARIABLE GALAXIES

In this section, we present MaNGA central spectra for a small sample of the mid-IR variable galaxies. We also present optical broad band images of the galaxy synthesized from the MaNGA data cube, and maps of the $H\alpha$ and [OIII]5007Å emission lines, showing the fluxes of those lines in the red and green channels, respectively. Finally, we plot the W2 light-curve of the galaxy to provide a comprehensive picture of the optical properties and mid-IR variability of the galaxy.

These figures can be found in Appendix A. Figure 11 shows where these objects lie in our variability space as well as W1 - W2 - sSFR space.

• 11981-6104: See the images of this galaxy in Fig. 12. This object has matches in both the MIRONG catalog and the Masterson et al. (2024) TDE catalog. Masterson

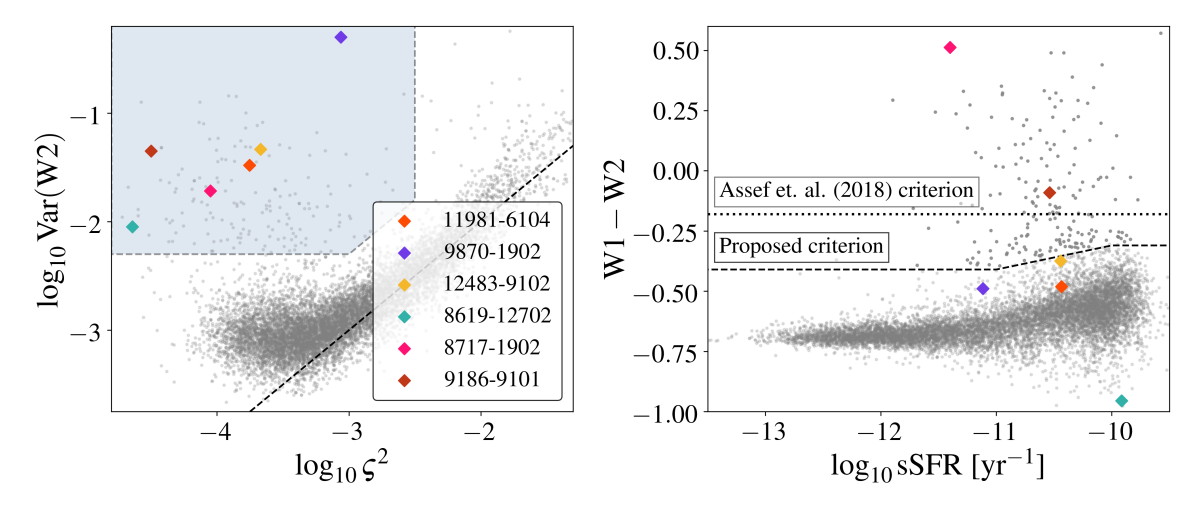


Figure 11. Showing where galaxies mentioned in Section 3 lie in our variability space (left panel) and in W1 - W2 vs. sSFR space (right panel). Each galaxy is labelled by a diamond and labelled by its plate-IFU.

et al. (2024) determines that it is a narrow line AGN (which we also find by our criteria) and for that reason rules it out as a TDE. In our stacked WISE images it has mid-IR colors consistent with stellar, but during the increase in brightness it becomes much redder (up to $W1-W2\sim0.5$), consistent with hot dust emission.

- 9870-1902: See the images of this galaxy in Fig. 12. This object has the highest observed variability of all our mid-IR variable galaxies. This galaxy does not appear in any other AGN classification scheme (it has LINER-like narrow line ratios). Like the previous example 11981-6104, it has stellar-like mid-IR colors before 2018, but during its bright phase has much redder colors indicative of hot dust.
- 12483-9102: See the images of this galaxy in Fig. 13. This object is the dwarf galaxy NGC 4395, which is a well-known low luminosity AGN host. It is red in W1 W2 colors (using our criterion) and is classified as a narrow-line AGN.
- **8619-12702**: See the images of this galaxy in Fig. 13. This object appears in the broadline AGN catalog.
- 8717-1902: See the images of this galaxy in Fig. 14. This object has one of the reddest W1-W2 colors in our sample. It does not manifest as an AGN in broad or narrow line classifications, though it is near the boundary of the narrow line AGN criterion in Figure 8, with $P1 \approx 0.10$ and $P3 \approx 0.47$.

• 9186-9101: See the images of this galaxy in Fig. 14. This object is red in W1 – W2 colors and appears in the broad-line catalog.

4. SUMMARY

We created a mid-IR variability catalog of galaxies, using the MaNGA component of SDSS-IV and their W2 light-curves from the NEOWISE and WISE All-Sky surveys. We used the observed variance across all epochs and compared it to the expected variance in W2 to identify variable objects, using the within-epoch variances in W2 to provide more accurate across-epoch expected variances. We used a Monte Carlo simulation to determine robust criteria for variability. We find that 170 galaxies satisfy these variability criteria. We also show that our catalog is roughly complete for variability with $\log_{10} \text{Var}(W2) > -2.3$ for galaxies with W2 < 16.5. The galaxies are listed in Appendix B.

We compare our catalog to existing broad-line and narrow-line AGN catalogs, MIRONG and TDE catalogs, and use traditional mid-IR AGN classification schemes such as the W1-W2 color to illuminate the demographics of the population of variable objects that we have selected. The majority of the variable objects ($\sim 80\%$) have other signatures of AGN activity.

As part of this work, we propose a modified W1 - W2 criterion for the MaNGA sample that provides a more complete sample of the population of AGN (Section 2.5.3).

5. DATA AVAILABILITY

The data used in this article (particularly in Fig. 3) have been tabulated in Appendix B. The W2

light-curves of all mid-IR variable galaxies have been plotted in Appendix C. The full MANGA-WISE variability catalog is available in the online supplementary material, which contains all of the statistical quantities calculated in Section 2.3 for all galaxies in MaNGA's DR17. A key between the names used in this article and the names in the file is also provided in Appendix B.

6. ACKNOWLEDGEMENTS

We thank David G. Grier, David W. Hogg, Or Graur, Sjoert Van Velzen and the IRSA helpdesk for useful conversations and guidance in writing this paper. AP acknowledges the support of the Dean's Undergraduate Research Fund from the College of Arts & Sciences at New York University.

This research has made use of the NASA/IPAC Infrared Science Archive, which is funded by the National Aeronautics and Space Administration and operated by the California Institute of Technology.

This publication makes use of data products from the Wide-field Infrared Survey Explorer, which is a joint project of the University of California, Los Angeles, and the Jet Propulsion Laboratory/California Institute of Technology, funded by the National Aeronautics and Space Administration.

This publication also makes use of data products from NEOWISE, which is a project of the Jet Propulsion Laboratory/California Institute of Technology, funded by the Planetary Science Division of the National Aeronautics and Space Administration.

Funding for the Sloan Digital Sky Survey IV has been provided by the Alfred P. Sloan Foundation, the U.S. Department of Energy Office of Science, and the Participating Institutions.

SDSS-IV acknowledges support and resources from the Center for High Performance Computing at the University of Utah. The SDSS website is www.sdss4.org.

SDSS-IV is managed by the Astrophysical Research Consortium for the Participating Institutions of the SDSS Collaboration including the Brazilian Participation Group, the Carnegie Institution for Science, Carnegie Mellon University, Center for Astrophysics — Harvard & Smithsonian, the Chilean Participation Group, the French Participation Group, Institute de Astrofísica de Canarias, The Johns Hopkins University, Kavli Institute for the Physics and Mathematics of the Uni-

verse (IPMU) / University of Tokyo, the Korean Participation Group, Lawrence Berkeley National Laboratory, Leibniz Institut für Astrophysik Potsdam (AIP), Max-Planck-Institut für Astronomie (MPIA Heidelberg), Max-Planck-Institut für Astrophysik (MPA Garching), Max-Planck-Institut für Extraterrestrische Physik (MPE), National Astronomical Observatories of China, New Mexico State University, New York University, University of Notre Dame, Observatário Nacional / MCTI, The Ohio State University, Pennsylvania State University, Shanghai Astronomical Observatory, United Kingdom Participation Group, Universidad Nacional Autónoma de México, University of Arizona, University of Colorado Boulder, University of Oxford, University of Portsmouth, University of Utah, University of Virginia, University of Washington, University of Wisconsin, Vanderbilt University, and Yale University.

Facility: IRSA, WISE

REFERENCES

- Abazajian, K. N., Adelman-McCarthy, J. K., Agüeros, M. A., et al. 2009, ApJS, 182, 543, doi: 10.1088/0067-0049/182/2/543
- Abdurro'uf, Accetta, K., Aerts, C., et al. 2022, The Astrophysical Journal Supplement Series, 259, 35, doi: 10.3847/1538-4365/ac4414
- Abolfathi, B., Aguado, D. S., Aguilar, G., et al. 2018, ApJS, 235, 42, doi: 10.3847/1538-4365/aa9e8a
- Antonucci, R. R. 1983, Nature, 303, 158
- Assef, R. J., Stern, D., Noirot, G., et al. 2018, The Astrophysical Journal Supplement Series, 234, 23, doi: 10.3847/1538-4365/aaa00a
- Baldwin, J. A., Phillips, M. M., & Terlevich, R. 1981,Publications of the Astronomical Society of thePacific, 93, 5, doi: 10.1086/130766
- Blanton, M. R., & Roweis, S. 2007, The Astronomical Journal, 133, 734–754, doi: 10.1086/510127
- Blanton, M. R., Bershady, M. A., Abolfathi, B., et al. 2017, The Astronomical Journal, 154, 28, doi: 10.3847/1538-3881/aa7567
- Bundy, K., Bershady, M. A., Law, D. R., et al. 2014, The Astrophysical Journal, 798, 7, doi: 10.1088/0004-637X/798/1/7
- Callow, J., Graur, O., Clark, P., et al. 2024, The rate of extreme coronal line emitting galaxies in the Sloan Digital Sky Survey and their relation to tidal disruption events. https://arxiv.org/abs/2402.16951
- Cherinka, B., Andrews, B. H., Sánchez-Gallego, J., et al. 2019, AJ, 158, 74,
- doi: 10.3847/1538-3881/ab2634
- Conroy, C., & Gunn, J. E. 2010, ApJ, 712, 833, doi: 10.1088/0004-637X/712/2/833
- Cook, D. O., Kasliwal, M. M., Sistine, A. V., et al. 2019, The Astrophysical Journal, 880, 7, doi: 10.3847/1538-4357/ab2131
- Dey, A., Schlegel, D. J., Lang, D., et al. 2019, AJ, 157, 168, doi: 10.3847/1538-3881/ab089d
- Drory, N., MacDonald, N., Bershady, M. A., et al. 2015, AJ, 149, 77, doi: 10.1088/0004-6256/149/2/77
- Fu, Y., Cappellari, M., Mao, S., et al. 2023, Monthly Notices of the Royal Astronomical Society, 524, 5827–5843, doi: 10.1093/mnras/stad2214

- Hickox, R. C., & Alexander, D. M. 2018, Annual Review of Astronomy and Astrophysics, 56, 625, doi: 10.1146/annurev-astro-081817-051803
- Ji, X., & Yan, R. 2020, Monthly Notices of the Royal Astronomical Society, 499, 5749
- Jiang, N., Wang, T., Dou, L., et al. 2021, The Astrophysical Journal Supplement Series, 252, 32, doi: 10.3847/1538-4365/abd1dc
- Law, D. R., Yan, R., Bershady, M. A., et al. 2015, AJ, 150, 19, doi: 10.1088/0004-6256/150/1/19
- Law, D. R., Cherinka, B., Yan, R., et al. 2016, AJ, 152, 83, doi: 10.3847/0004-6256/152/4/83
- Lyu, J., & Rieke, G. 2022, Universe, 8, 304, doi: 10.3390/universe8060304
- Mainzer, A., Bauer, J., Cutri, R. M., et al. 2014, ApJ, 792, 30, doi: 10.1088/0004-637X/792/1/30
- Masterson, M., De, K., Panagiotou, C., et al. 2024, The Astrophysical Journal, 961, 211, doi: 10.3847/1538-4357/ad18bb
- Morrissey, P., Conrow, T., Barlow, T. A., et al. 2007, ApJS, 173, 682, doi: 10.1086/520512
- Nenkova, M., Sirocky, M. M., Nikutta, R., Ivezić, Ž., & Elitzur, M. 2008, ApJ, 685, 160, doi: 10.1086/590483
- Oke, J. B., & Schild, R. E. 1970, ApJ, 161, 1015, doi: 10.1086/150603
- Pedregosa, F., Varoquaux, G., Gramfort, A., et al. 2011, Journal of Machine Learning Research, 12, 2825
- Sánchez, S. F., Barrera-Ballesteros, J. K., Lacerda, E., et al. 2022, ApJS, 262, 36, doi: 10.3847/1538-4365/ac7b8f
- Smee, S. A., Gunn, J. E., Uomoto, A., et al. 2013, The Astronomical Journal, 146, 32
- Smith, J. D. T., Draine, B. T., Dale, D. A., et al. 2007, ApJ, 656, 770, doi: 10.1086/510549
- Stern, D., Assef, R. J., Benford, D. J., et al. 2012, The Astrophysical Journal, 753, 30, doi: 10.1088/0004-637X/753/1/30
- Veilleux, S., & Osterbrock, D. E. 1987, ApJS, 63, 295, doi: 10.1086/191166
- Wang, T.-G., Zhou, H.-Y., Komossa, S., et al. 2012, The Astrophysical Journal, 749, 115, doi: 10.1088/0004-637X/749/2/115
- Westfall, K. B., Cappellari, M., Bershady, M. A., et al. 2019, AJ, 158, 231, doi: 10.3847/1538-3881/ab44a2
- Wright, E. L., Eisenhardt, P. R. M., Mainzer, A. K., et al. 2010, AJ, 140, 1868,
 - doi: 10.1088/0004-6256/140/6/1868

APPENDIX

A. VARIABLE GALAXY IMAGES

Here, we provide images, spectra and W2 light-curves of the galaxies mentioned in Section 3. The images and spectra were obtained using the SDSS Marvin tool (Cherinka et al. 2019).

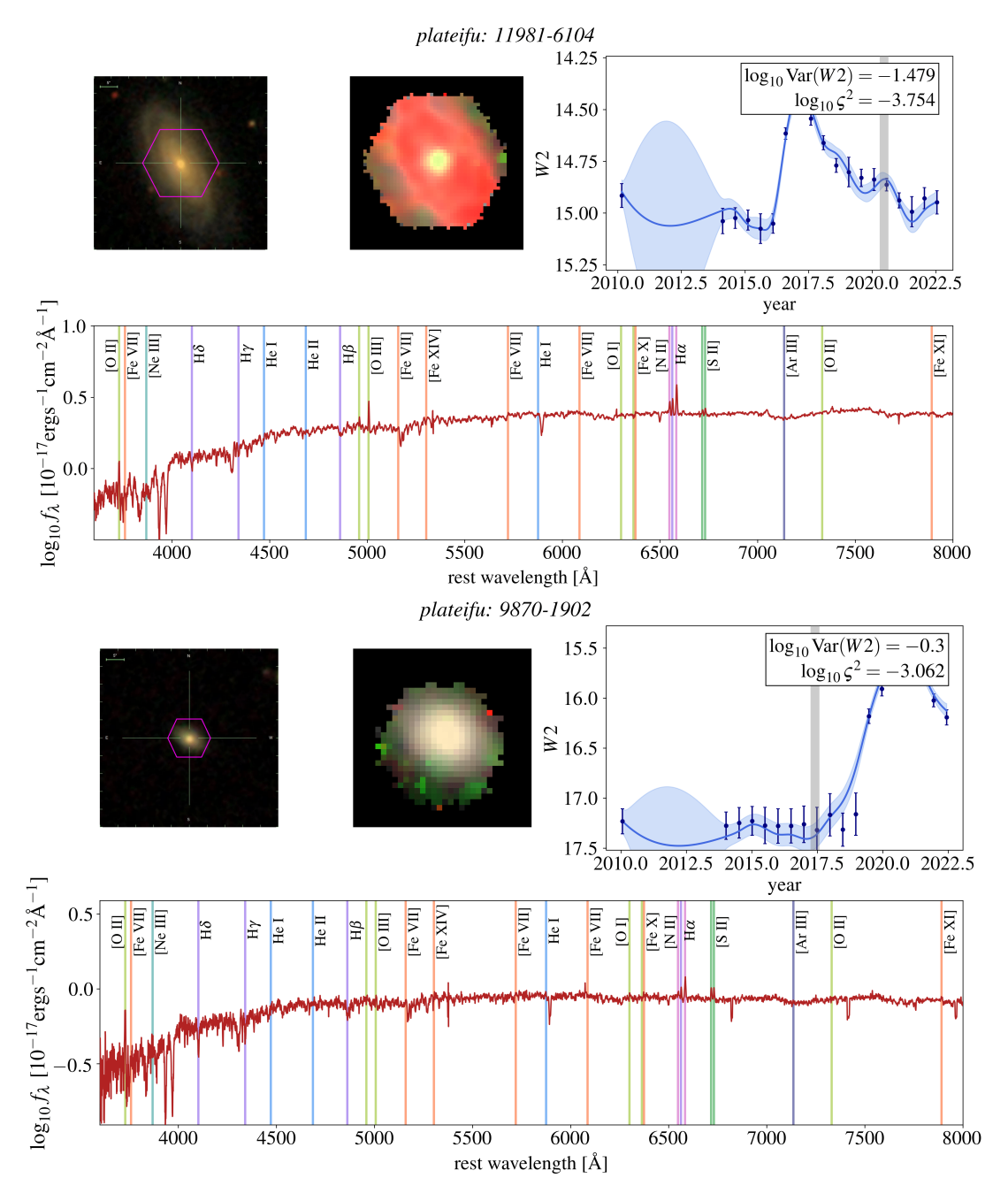


Figure 12. Images and spectra of galaxies 11981-6104 and 9870-1902. For each galaxy, the top left panel shows the SDSS optical image of the galaxy, the top center panel shows the H α (red) and [OIII] (green) maps overlaid on the r-band flux (grey). The top right panel shows the W2 light-curve (the grey line indicates when it was observed by MaNGA). The bottom panel shows the MaNGA spectra with emission lines marked. Lines from the same element are of the same color.

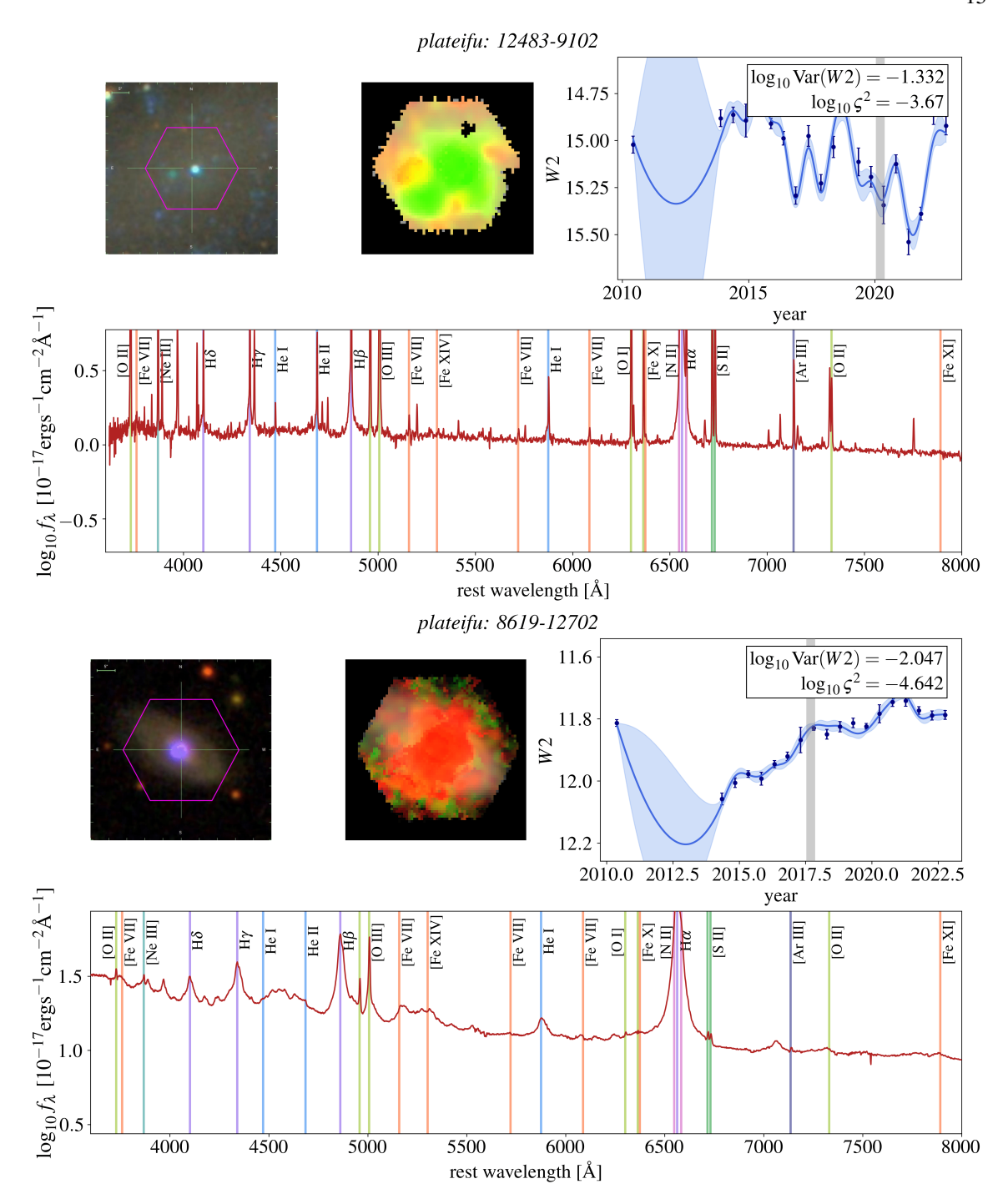


Figure 13. Similar to Figure 12, for plate-IFUs 12483-9102 and 8619-12702. Plate-IFU 12483-9102 observed the center of NGC 4395, which is a well-known low mass AGN hosting dwarf galaxy. The image and MaNGA data cube only cover the central region of the whole galaxy, which subtends a large solid angle on the sky.

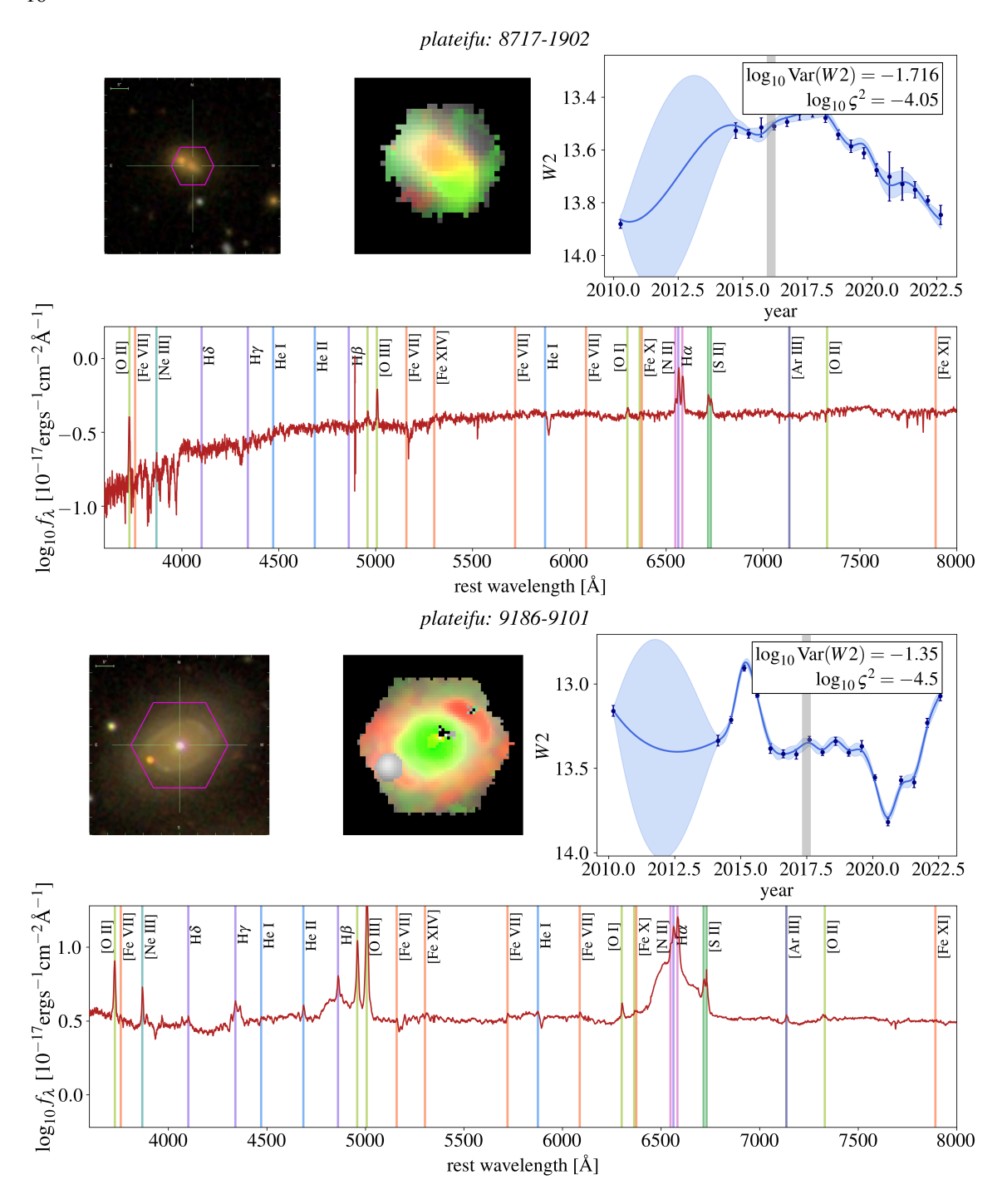


Figure 14. Similar to Figure 12, for plate-IFUs 8717-1902 and 9186-9101.

B. THE MANGA-WISE VARIABILITY CATALOG

Table 2 provides a key between the column labels in the variability catalog and the statistical quantities calculated in Section 2.3. Here, 'W?' can be either W1 or W2. Table 3 lists all of the objects that we identify as variable in the mid-IR.

Table 2. MANGA-WISE variability catalog key

Column in FITS file	Quantity	Units	Description
plateifu	Plateifu	_	Identifier from MaNGA catalog
ra	RA	J2000	Right Ascension of galaxy
dec	Declination	J2000	Declination of galaxy
mjd	Epoch date	days	Modified Julian Date of each epoch
obs_per_ep	n	_	Number of observations per epoch
epochs_count	N	_	Number of epochs
mean_W?_per_epoch	\overline{W} ?	mag	mean of the W? observations in each epoch
err_W?_per_epoch	$\sigma_{\overline{ m W?}}$	mag	error per epoch
expected_var_W?_errs	$\sigma_{ m ep}^2$	mag ²	expected variance per epoch
	-		based on catalog uncertainties
expected_var_W?_mags	Var(W?ep)	mag ²	expected variance per epoch
			calculated from within-epoch W? magnitudes
expected_W?_var_mean_errs	σ_i^2	mag ²	expected variance in the mean per epoch
			based on catalog uncertainties
expected_W?_var_mean_mags	ς_j^2	mag ²	expected variance in the mean per epoch
			based on within-epoch W? magnitudes
observed_W?_var	Var(W?)	mag ²	observed variance across all epochs
			of the mean magnitudes per epoch
expected_W?_var_all_errs	σ^2	mag ²	expected variance across all epochs
			based on catalog uncertainties
expected_W?_var_all_mags	ς^2	mag ²	expected variance across all epochs based on within epoch
			variances calculated from W? magnitudes
vi_flag	_	_	1 if we believe the WISE variability to be questionable,
			0 otherwise. We only visually inspected galaxies identified
			as variable by our criteria.
epoch_flag	_	_	1 if the galaxy has 3 or fewer epochs, 0 otherwise
var_flag	_	_	1 if the object is variable in the mid-IR, 0 otherwise

Table 3. The MANGA-WISE variability catalog

Plateifu	RA	Dec	W1	W2	$\log_{10} \varsigma^2$	$\log_{10} \text{Var}(W2)$
	(deg)	(deg)	(AB mag)	(AB mag)	$(AB \ mag^2)$	$(AB mag^2)$
8091-6101	11.8308	14.7035	13.62	13.85	-4.058	-1.239
8091-9101	11.8765	15.6971	14.41	15.02	-3.628	-1.851

Table 3 continued

 $Table\ 3\ (continued)$

	Table 3 (continuea)								
Plateifu	RA	Dec	W1	W2	$\log_{10} \varsigma^2$	$\log_{10} \text{Var}(W2)$			
	(deg)	(deg)	(AB mag)	(AB mag)	$(AB mag^2)$	$(AB mag^2)$			
8091-12702	12.4139	13.6852	14.96	14.76	-3.638	-2.222			
12073-3704	14.6979	-1.0971	14.78	14.73	-3.82	-1.254			
8093-9102	20.8484	15.2147	13.9	14.52	-3.071	-1.936			
12078-6102	29.1378	-0.175	14.7	15.38	-3.306	-1.831			
10223-3701	31.5666	-0.2914	13.08	13.25	-3.854	-0.845			
9514-1901	33.24	14.1028	14.58	14.76	-3.601	-1.856			
10222-12701	43.0975	-8.5104	13.03	13.02	-3.935	-1.427			
9193-9101	46.2942	-1.0755	15.64	16.14	-3.579	-2.073			
9193-12704	46.6649	0.062	15.34	15.16	-3.89	-1.62			
8158-3704	61.4533	-6.3238	16.23	16.7	-2.761	-1.815			
8132-6102	111.1382	41.9506	15.21	15.92	-2.993	-1.668			
8132-6101	111.7337	41.0267	15.09	15.42	-3.481	-1.623			
8133-12702	113.5109	43.5436	_	_	-3.3	-1.879			
8726-12701	115.717	22.1127	14.61	15.15	-3.137	-2.269			
8145-6102	116.5535	26.923	15.58	16.05	-2.585	-0.823			
8710-6102	117.9662	49.8143	13.91	14.27	-3.913	-0.84			
9497-12705	118.0743	19.5951	_	_	-3.408	-1.743			
8717-1902	118.0911	34.3266	14.97	14.32	-4.05	-1.716			
10216-12704	118.1623	18.3216	14.47	14.91	-3.522	-1.767			
8714-3704	118.1842	45.9493	14.29	14.61	-4.117	-1.819			
10217-3704	118.3957	14.4733	15.05	15.62	-2.75	-1.921			
10218-12703	118.6342	16.8097	13.38	13.76	-3.59	-2.283			
9182-12703	118.7745	40.0413	15.46	15.83	-3.412	-2.26			
8713-9102	118.8554	39.1861	14.61	14.7	-3.891	-2.02			
8718-12701	119.1822	44.8567	15.62	16.09	-3.139	-1.744			
9503-12701	119.9728	23.3901	12.41	12.42	-4.03	-1.724			
9498-3703	120.0169	23.4378	13.99	14.42	-3.848	-1.858			
8940-12702	120.0874	26.6135	12.66	12.66	-4.137	-1.085			
9183-3703	121.9208	39.0042	14.69	14.87	-4.082	-1.98			
9487-3702	123.3305	46.1472	15.31	15.71	-3.525	-1.291			
9487-9102	123.8203	46.0753	13.69	13.79	-4.359	-2.009			
10493-1902	124.3274	52.0299	16.85	16.82	-3.449	-1.756			
8723-3702	127.0444	55.7124	13.51	13.96	-3.82	-2.15			
9508-12704	127.106	26.3974	15.71	16.05	-3.45	-2.267			
8241-9102	127.1708	17.5814	14.34	14.47	-4.174	-1.789			
8725-9102	127.1781	45.7426	15.18	15.47	-3.451	-1.319			
11746-12704	127.7849	30.8956	15.08	15.45	-3.242	-1.864			
9507-12705	129.5207	25.3295	14.36	14.88	-3.326	-2.155			
9502-12703	129.5456	24.8953	13.06	13.47	-3.563	-1.699			
10498-6101	129.747	26.137	13.49	13.54	-3.603	-1.808			
11747-12703	130.0098	29.8174	15.42	15.11	-3.878	-2.054			

Table 3 continued

 Table 3 (continued)

Plateifu	RA	Dec	W1	W2	$\log_{10} \varsigma^2$	$log_{10} Var(W2)$
	(deg)	(deg)	(AB mag)	(AB mag)	(AB mag ²)	(AB mag ²)
8723-6104	130.4078	54.9186	13.96	13.81	-3.701	-1.449
12511-12705	133.9486	0.7943	13.43	13.25	-4.339	-2.18
12511-3701	133.9762	0.8531	14.83	14.9	-3.784	-1.136
12511-3702	134.6499	1.5304	15.11	15.44	-3.802	-2.068
10500-12703	137.1602	32.593	13.11	13.7	-3.972	-2.175
8152-9102	144.1565	34.4774	16.21	16.79	-3.424	-2.106
12512-12702	146.3735	-0.3652	14.35	14.59	-3.436	-2.164
10515-6102	147.4028	4.1163	14.89	15.43	-2.879	-2.133
10845-12701	147.9806	3.4834	14.87	15.2	-3.625	-1.882
10516-12701	150.5293	3.0577	13.63	14.09	-4.074	-1.845
10846-6104	154.5278	0.0999	14.47	14.8	-3.704	-2.164
11838-12703	156.5881	0.6849	13.37	13.07	-4.422	-1.318
11865-1901	156.5881	0.6849	13.36	13.07	-4.422	-1.318
11838-1902	156.7275	-0.5415	15.3	15.76	-3.872	-1.826
10837-3701	160.1437	0.8174	14.28	14.75	-3.454	-1.969
8999-3702	163.4339	49.4989	14.98	15.33	-3.612	-2.045
8998-12705	163.6638	47.8623	15.73	16.13	-3.523	-1.867
8947-3701	168.9478	50.4016	15.51	15.21	-4.043	-2.269
8466-3704	169.5134	45.113	14.67	14.96	-3.936	-1.717
9000-1901	171.4007	54.3826	13.79	13.75	-4.575	-0.898
8992-3702	171.6573	51.573	15.23	15.63	-2.59	-1.833
8992-12702	172.3172	51.5232	14.02	14.39	-4.005	-1.341
8990-12705	173.5376	49.2546	16.24	16.59	-3.243	-1.178
8310-3701	179.2945	22.2962	15.27	15.43	-3.656	-1.916
8260-9101	182.2867	44.0032	13.95	14.24	-3.785	-1.309
11833-3702	184.0295	50.8251	13.69	14.1	-4.265	-1.514
8262-9101	184.5438	44.4005	13.85	14.37	-3.922	-2.164
12483-9102	186.454	33.5469	14.22	14.49	-3.67	-1.332
8341-12704	189.2133	45.6512	17.85	18.23	-3.781	-0.997
11014-9101	192.0387	26.9392	14.19	14.46	-3.992	-1.635
11863-3703	194.0593	56.8734	_	_	-3.403	-2.137
11954-1901	196.5874	53.3064	14.9	15.38	-3.76	-2.115
8318-3704	197.8918	44.9331	14.48	14.91	-3.821	-2.109
12514-6103	198.2742	1.4655	17.19	17.75	-3.179	-2.183
11830-1902	198.7493	51.2726	15.23	15.53	-3.696	-1.112
8322-3701	199.0665	30.2645	14.5	14.88	-3.799	-1.835
12514-9102	199.2706	1.828	14.29	14.62	-3.597	-1.899
8445-3701	205.6425	35.0203	13.64	14.2	-3.533	-1.994
8446-1901	205.7533	36.1657	15.86	15.94	-3.965	-1.423
8983-3704	206.0079	25.9412	14.97	15.28	-3.469	-2.024
8447-9102	207.4544	40.5374	14.53	15.0	-2.669	-1.707

Table 3 continued

 $Table\ 3\ (continued)$

Table 3 (continuea)								
Plateifu	RA	Dec	W1	W2	$\log_{10} \varsigma^2$	$\log_{10} \text{Var}(W2)$		
	(deg)	(deg)	(AB mag)	(AB mag)	$(AB mag^2)$	$(AB mag^2)$		
8334-3703	213.2302	39.3127	15.03	15.6	-3.536	-2.164		
8337-1901	214.0964	38.191	15.28	15.59	-3.27	-1.946		
8333-12705	214.2842	42.6828	16.77	17.42	-2.642	-1.924		
8326-6102	215.0179	47.1213	14.75	14.86	-4.184	-1.81		
8333-3703	215.4497	42.3279	15.66	16.14	-3.14	-2.074		
8547-12701	217.63	52.7072	13.92	14.29	-4.319	-1.726		
11011-1902	218.7186	48.6619	15.42	15.63	-4.131	-0.897		
9867-6104	220.8804	49.3931	13.95	14.38	-4.069	-2.112		
11835-12705	220.9555	1.926	14.24	14.71	-3.331	-2.215		
9024-12705	223.8675	32.84	15.58	16.13	-2.717	-1.328		
8593-12705	226.9375	51.4528	13.61	13.92	-4.293	-1.566		
8596-12702	230.1723	49.1065	13.63	13.91	-4.174	-1.621		
8598-9102	230.1723	49.1065	13.63	13.91	-4.174	-1.621		
9890-1901	232.4191	30.4859	14.91	14.93	-3.817	-1.82		
9870-1902	233.1651	44.5342	17.09	17.53	-3.062	-0.3		
9870-9101	233.2834	44.5357	14.67	15.23	-3.747	-1.311		
8553-1901	233.9683	57.9026	13.74	13.48	-4.599	-1.945		
8488-12702	234.3747	46.8641	15.02	15.51	-3.406	-2.221		
9889-12705	235.9988	24.9985	15.78	16.12	-2.724	-1.636		
11974-12701	237.477	8.8612	15.21	15.68	-2.864	-1.562		
8546-6103	237.6516	51.398	14.96	14.89	-4.191	-1.699		
8564-3701	238.8712	47.3172	15.42	15.88	-3.491	-2.149		
11974-3702	239.0804	9.8154	13.94	14.21	-3.994	-1.447		
9887-1901	239.1785	29.8132	17.85	17.83	-4.311	-1.694		
9094-6101	239.4314	27.4647	14.14	14.4	-3.992	-1.23		
8487-9102	240.2142	46.4814	16.13	16.72	-3.165	-1.857		
8549-12701	240.4709	45.3519	14.49	14.97	-4.172	-2.202		
9032-12701	240.4751	31.8921	14.09	14.34	-3.157	-1.672		
8313-6101	240.6581	41.2934	14.55	15.04	-3.868	-1.442		
9031-12705	241.151	43.8798	15.9	16.39	-3.379	-1.831		
9036-6101	241.151	43.8798	15.86	16.36	-3.379	-1.831		
9885-3703	241.1527	23.6632	14.24	14.79	-3.873	-2.242		
9087-6101	241.1933	21.9573	15.18	15.0	-4.338	-1.988		
8549-12702	241.2714	45.443	14.01	14.4	-4.132	-1.595		
8561-3704	241.3254	52.1202	16.93	17.32	-3.656	-1.084		
9032-12702	241.4528	30.7171	15.76	16.29	-3.07	-2.004		
9090-3701	241.7174	27.9275	15.11	15.0	-4.363	-1.641		
9091-3704	241.9447	25.5375	15.88	15.71	-3.601	-2.137		
9030-12702	242.3324	30.0108	15.61	16.01	-3.435	-2.063		
11944-12704	243.2568	37.2875	14.4	14.37	-3.298	-1.389		
8314-1902	243.259	39.2371	14.06	14.53	-4.025	-2.184		

Table 3 continued

Table 3 (continued)

Table 3 (Commune)								
Plateifu	RA	Dec	W1	W2	$\log_{10} \varsigma^2$	$\log_{10} \text{Var}(W2)$		
	(deg)	(deg)	(AB mag)	(AB mag)	(AB mag ²)	(AB mag ²)		
9046-1902	243.555	26.0712	_	_	-4.517	-2.123		
9027-12701	243.9359	31.964	13.63	14.11	-3.652	-2.257		
8562-6102	244.1027	51.9498	14.25	14.75	-4.033	-2.27		
8483-12701	244.1881	48.6003	16.51	16.82	-3.309	-1.592		
9048-1902	246.256	24.2632	15.66	16.01	-3.604	-1.392		
11940-12704	246.9641	36.1556	13.89	13.85	-4.313	-2.102		
9892-6102	247.4704	24.444	14.49	15.0	-4.077	-1.706		
11943-6104	247.636	39.3842	13.97	14.09	-4.385	-1.975		
9892-12702	247.8147	23.8826	14.83	14.8	-4.0	-1.595		
9892-3703	248.3839	24.9847	15.19	15.52	-3.469	-1.931		
11757-3702	248.4313	26.329	14.91	15.16	-3.756	-2.086		
11757-12704	249.5572	26.2818	13.86	14.32	-3.798	-1.982		
12667-6104	249.9323	36.7008	16.22	16.5	-3.077	-2.042		
11978-6103	250.2818	22.8236	15.51	15.94	-3.18	-1.346		
8978-6104	251.3359	42.7578	17.2	17.67	-3.363	-2.195		
12651-3703	252.1943	27.0105	15.82	16.5	-2.838	-2.089		
11979-6104	253.048	22.7565	14.56	15.17	-3.492	-2.229		
8612-1901	253.4676	39.7602	12.13	12.47	-4.719	-1.957		
11981-3703	254.4339	19.3687	16.32	16.28	-3.337	-1.88		
11981-6104	254.8444	20.8298	13.86	14.35	-3.754	-1.479		
7959-6103	256.2832	30.4032	14.72	15.11	-4.255	-2.038		
8614-12703	258.1185	35.8841	13.9	14.29	-4.085	-1.677		
7958-9101	258.4958	33.6071	15.53	15.87	-3.371	-2.07		
7991-6104	258.8274	57.6588	14.37	14.9	-3.851	-1.838		
9186-9101	260.6664	30.8813	13.15	13.21	-4.5	-1.35		
9196-12703	262.3993	54.4944	14.42	14.53	-4.599	-1.888		
8624-3702	263.0508	59.9415	13.29	13.67	-4.674	-1.683		
8626-12702	263.2054	56.9013	14.38	14.95	-4.265	-1.918		
7972-3704	316.8413	11.0664	15.99	16.2	-3.023	-1.378		
7815-6104	319.1931	11.0437	14.98	14.97	-3.963	-1.984		
8615-3701	321.0079	-0.3663	14.99	15.21	-3.709	-1.732		
8616-12701	322.2532	0.1826	15.75	16.34	-2.961	-2.138		
8619-3701	322.9334	11.3812	16.45	16.78	-3.559	-1.707		
8619-12702	323.1159	10.1386	15.29	16.01	-4.642	-2.047		
12683-6102	325.5908	-8.3649	15.43	15.86	-2.996	-1.946		
7977-9101	331.1229	12.4426	13.81	14.2	-4.101	-1.097		
7981-9102	338.4101	13.2121	14.84	14.86	-4.031	-1.962		
7981-3703	339.2821	14.232	13.83	14.14	-3.213	-2.276		
12071-1901	345.9218	1.0436	14.4	14.15	-3.841	-2.147		
12085-6103	345.9294	13.9265	14.06	14.52	-3.828	-2.194		
12071-12702	346.3285	0.1895	12.36	12.31	-4.367	-2.184		

Table 3 continued

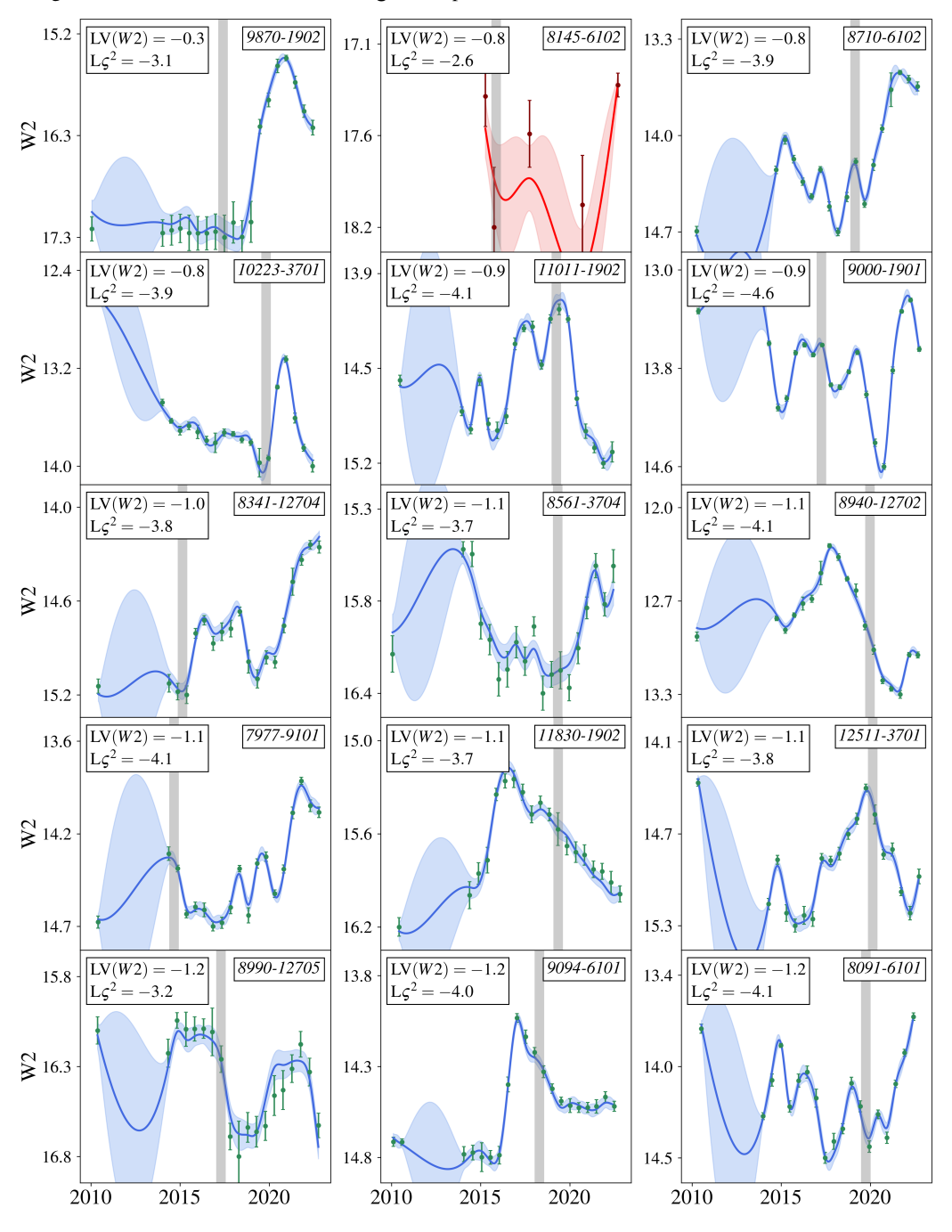
 Table 3 (continued)

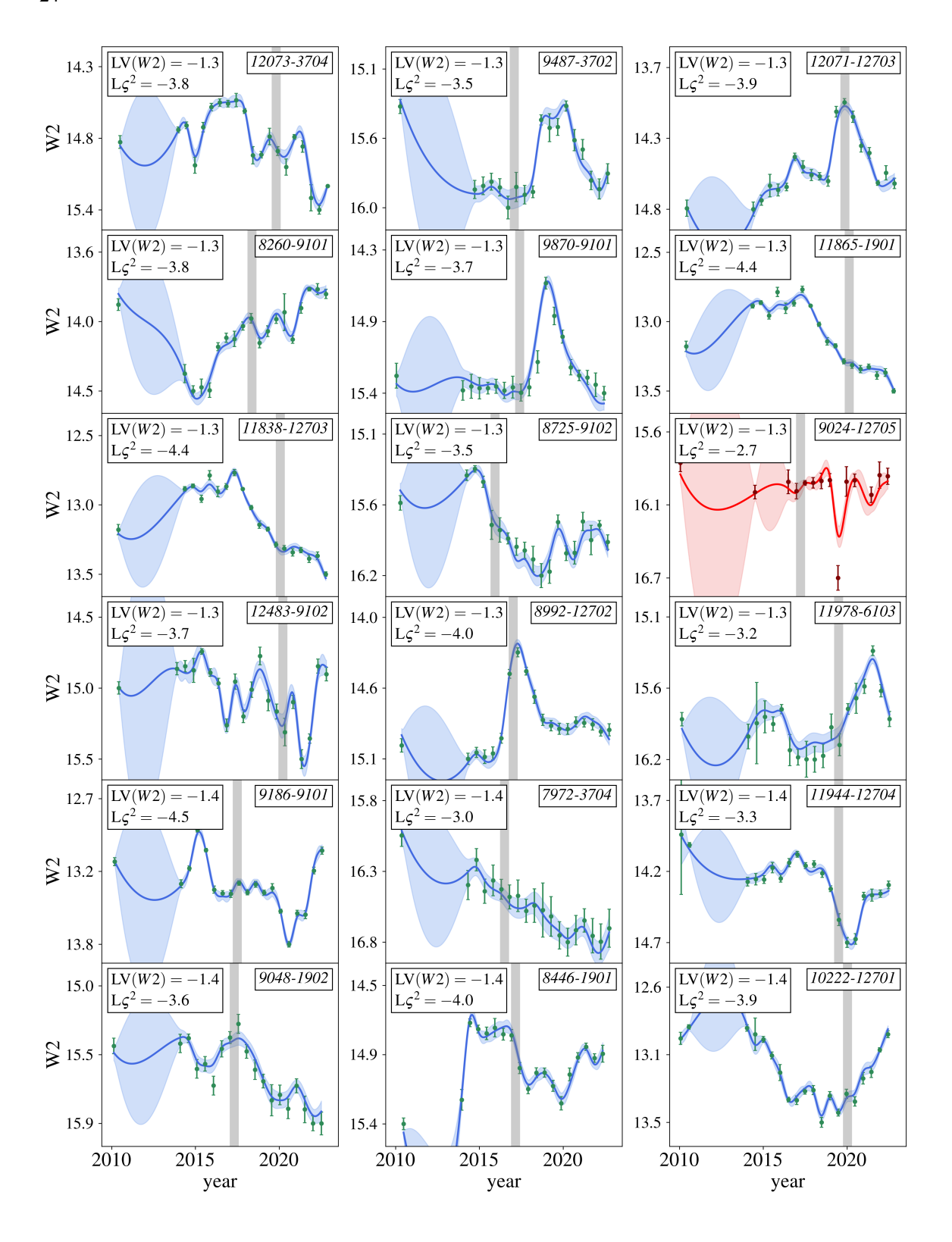
Plateifu	RA	Dec	W1	W2	$\log_{10} \varsigma^2$	$\log_{10} \operatorname{Var}(W2)$
	(deg)	(deg)	(AB mag)	(AB mag)	$(AB mag^2)$	$(AB mag^2)$
12085-1902	346.5688	14.429	16.33	17.02	-2.989	-1.971
12071-12703	347.3345	0.7565	16.0	16.38	-3.865	-1.304
12088-3701	348.4187	14.021	13.37	13.48	-4.05	-1.918
12089-6104	351.8415	15.4104	13.46	13.53	-4.428	-1.616

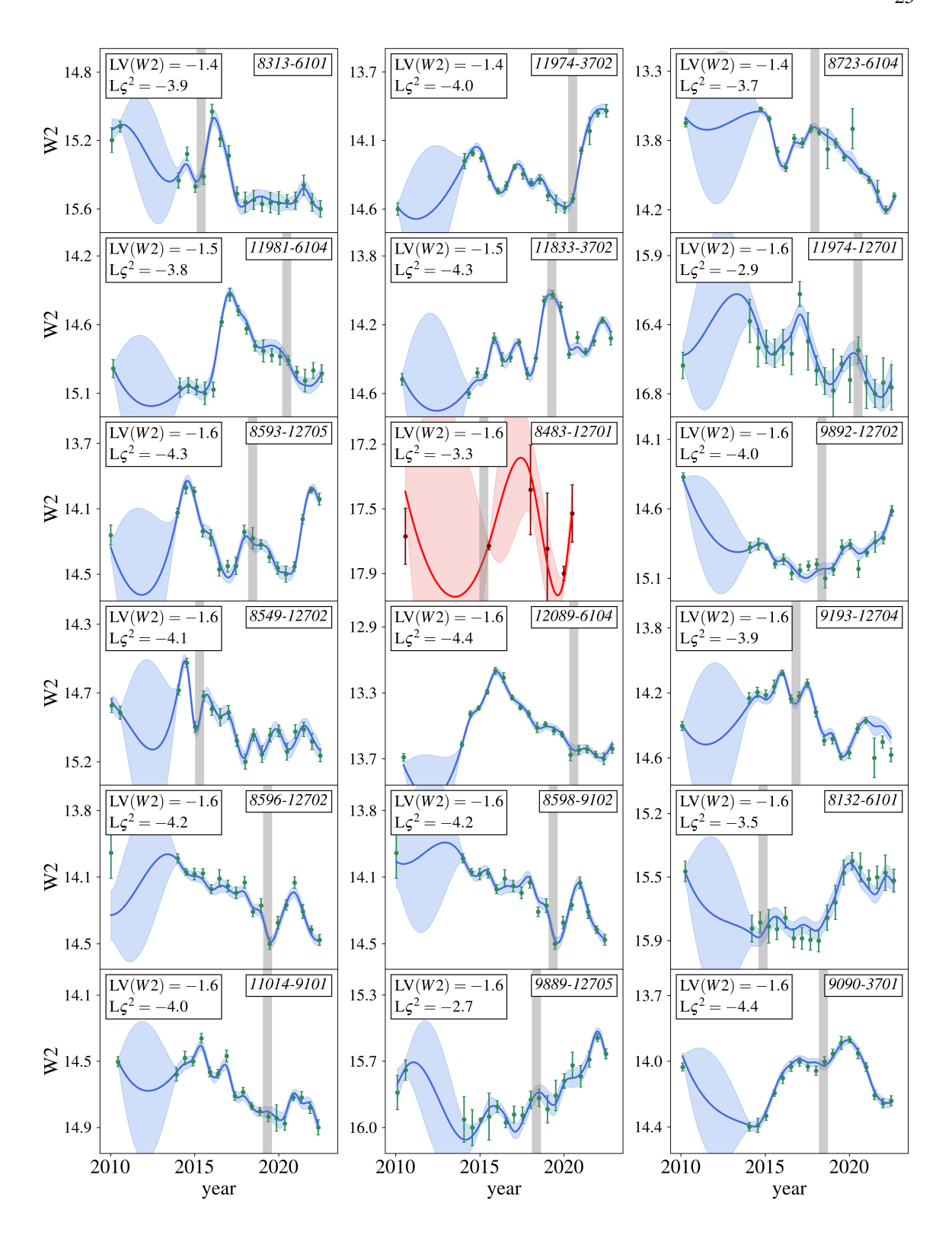
C. MID-IR VARIABLE GALAXY LIGHT-CURVES

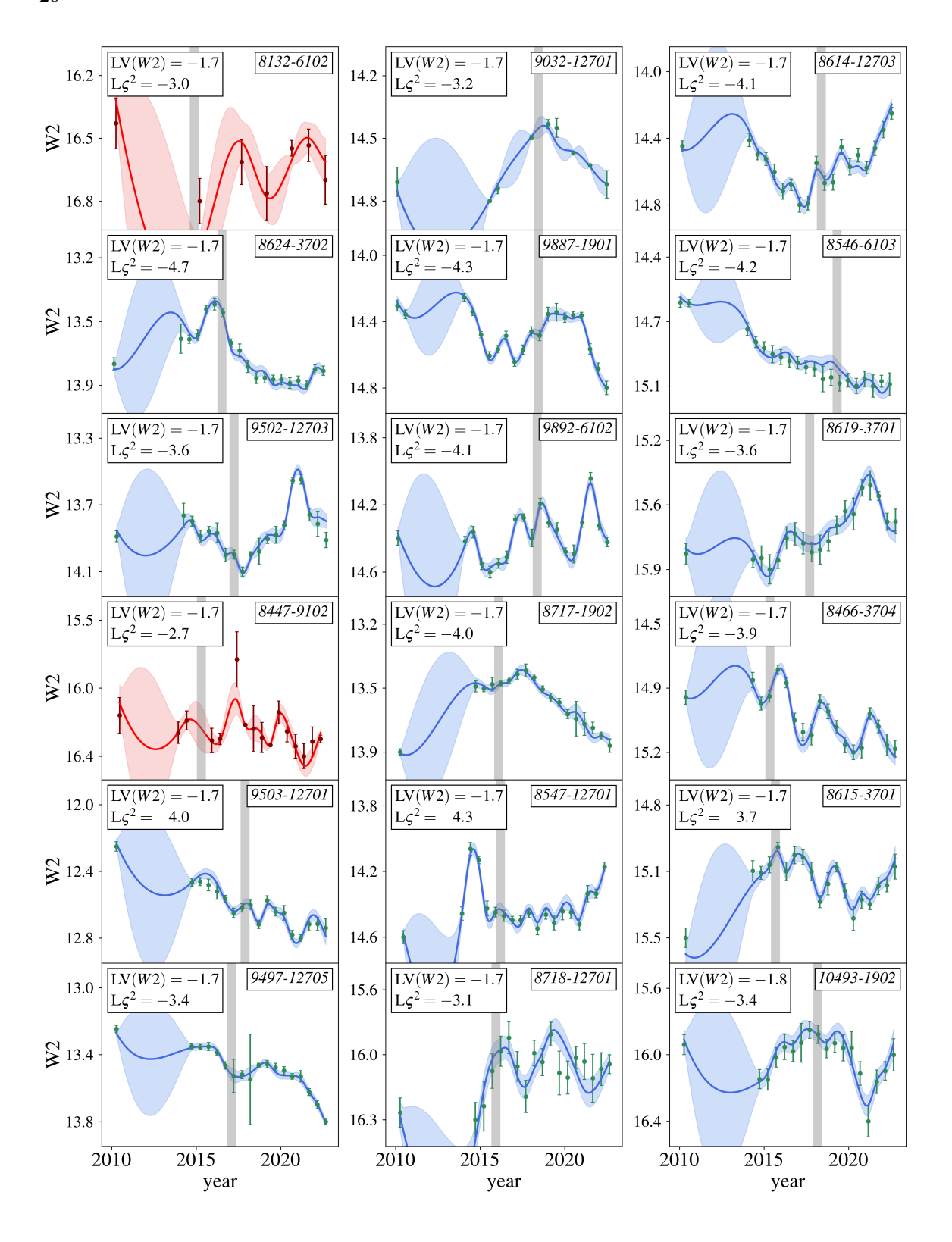
We plot the W2 light-curves ordered by decreasing $\log_{10} \text{Var}(W2)$. To interpolate between observations we perform Gaussian process regression with the scikit-learn Python package, using a Matern-3/2 kernel with a length scale hyperparameter of ~ 15 years. Light-curves of galaxies which have the vi_flag set are plotted in red. The gray bands mark the dates of the MaNGA observations.

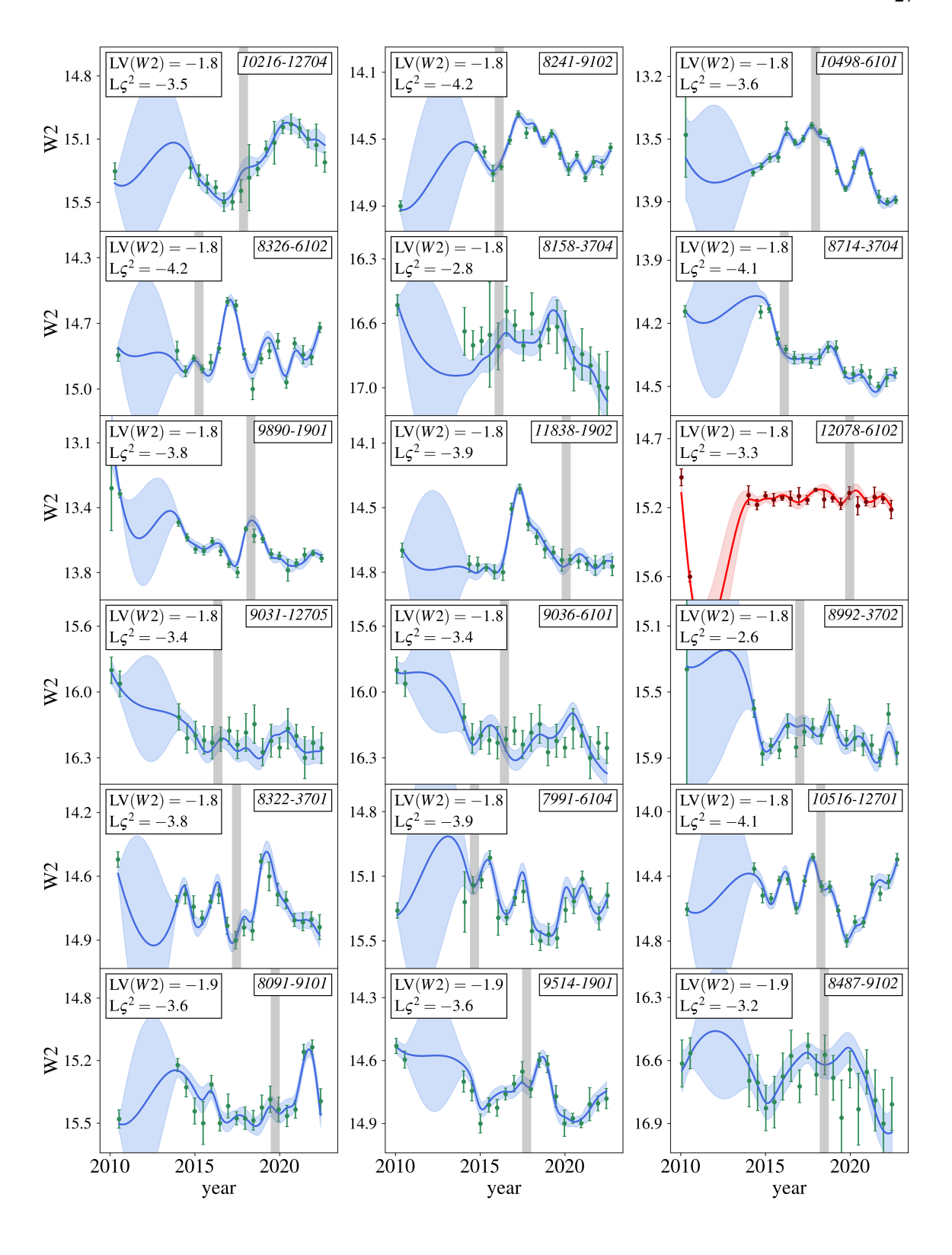
Figure 15. W2 light-curves of mid-IR variable galaxies, ordered by $\log_{10} \text{Var}(W2)$ and labelled by MaNGA plate-IFU (top right). They are also labelled by their coordinates on our variability space (top left), where $\text{LV}(W2) \equiv \log_{10} \text{Var}(W2)$ and $\text{L}\zeta^2 \equiv \log_{10} \zeta^2$. The grey line marks when MaNGA observed the galaxy. The blue line and band show the Gaussian process regression fit. Galaxies with the vi_flag set are plotted in red.

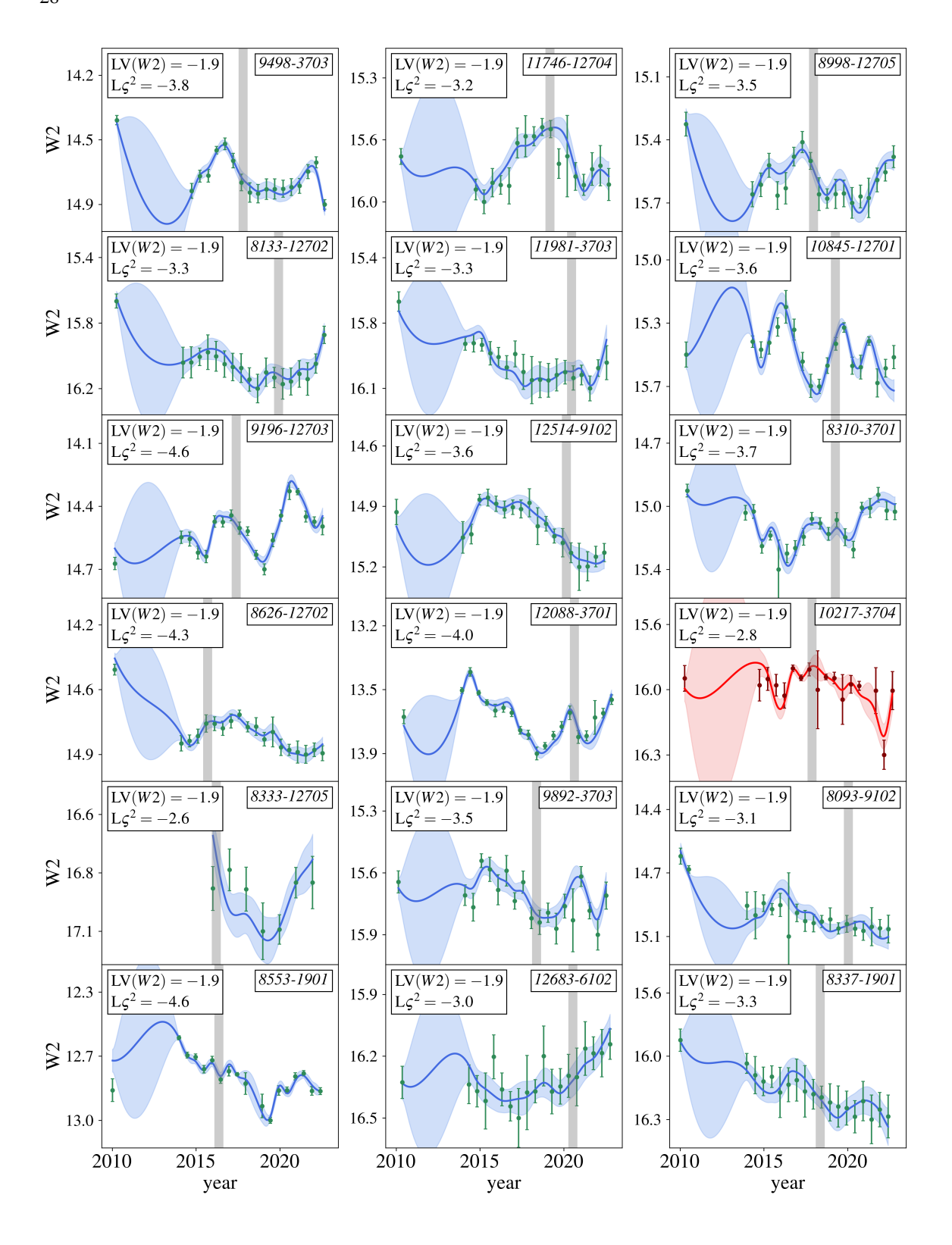


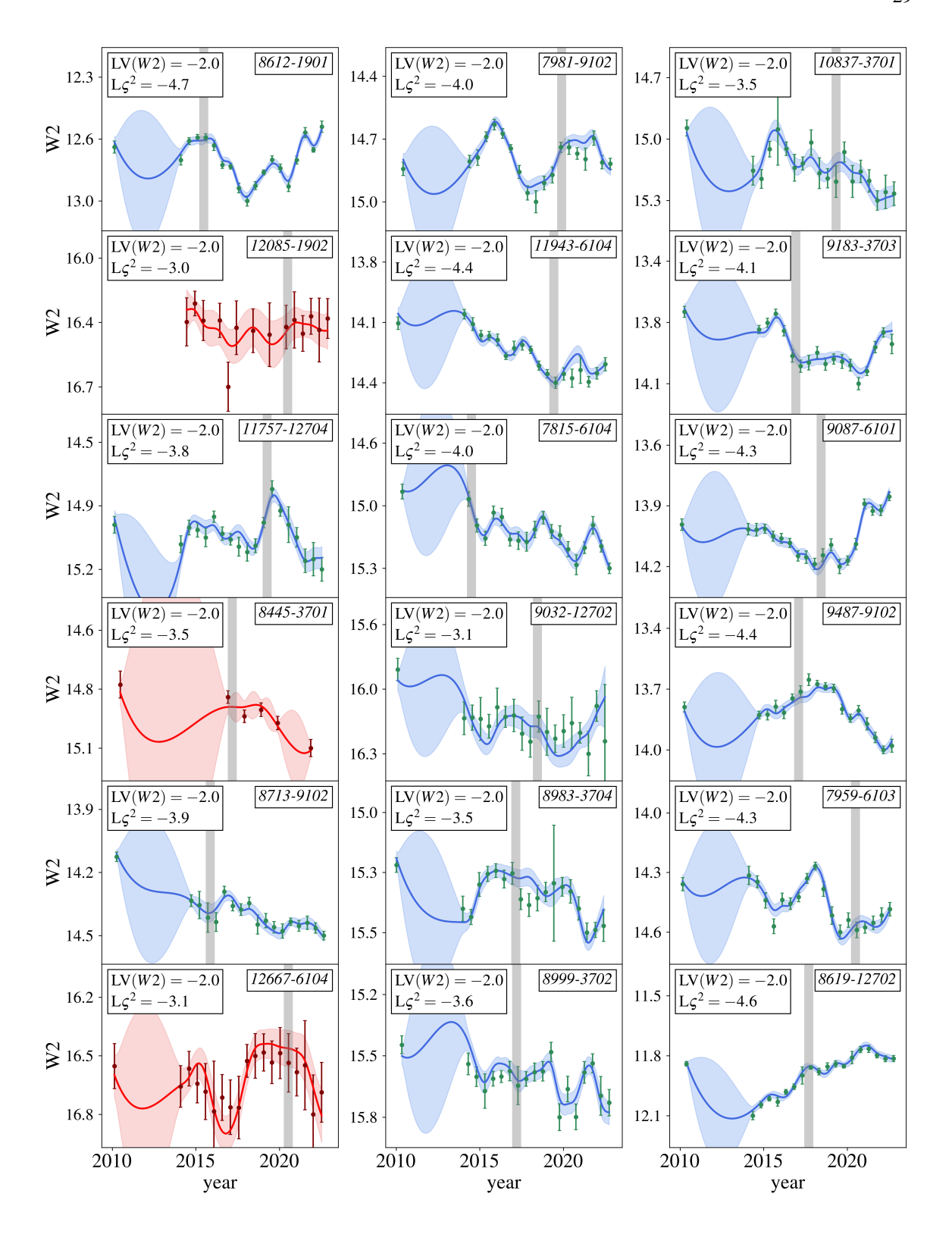


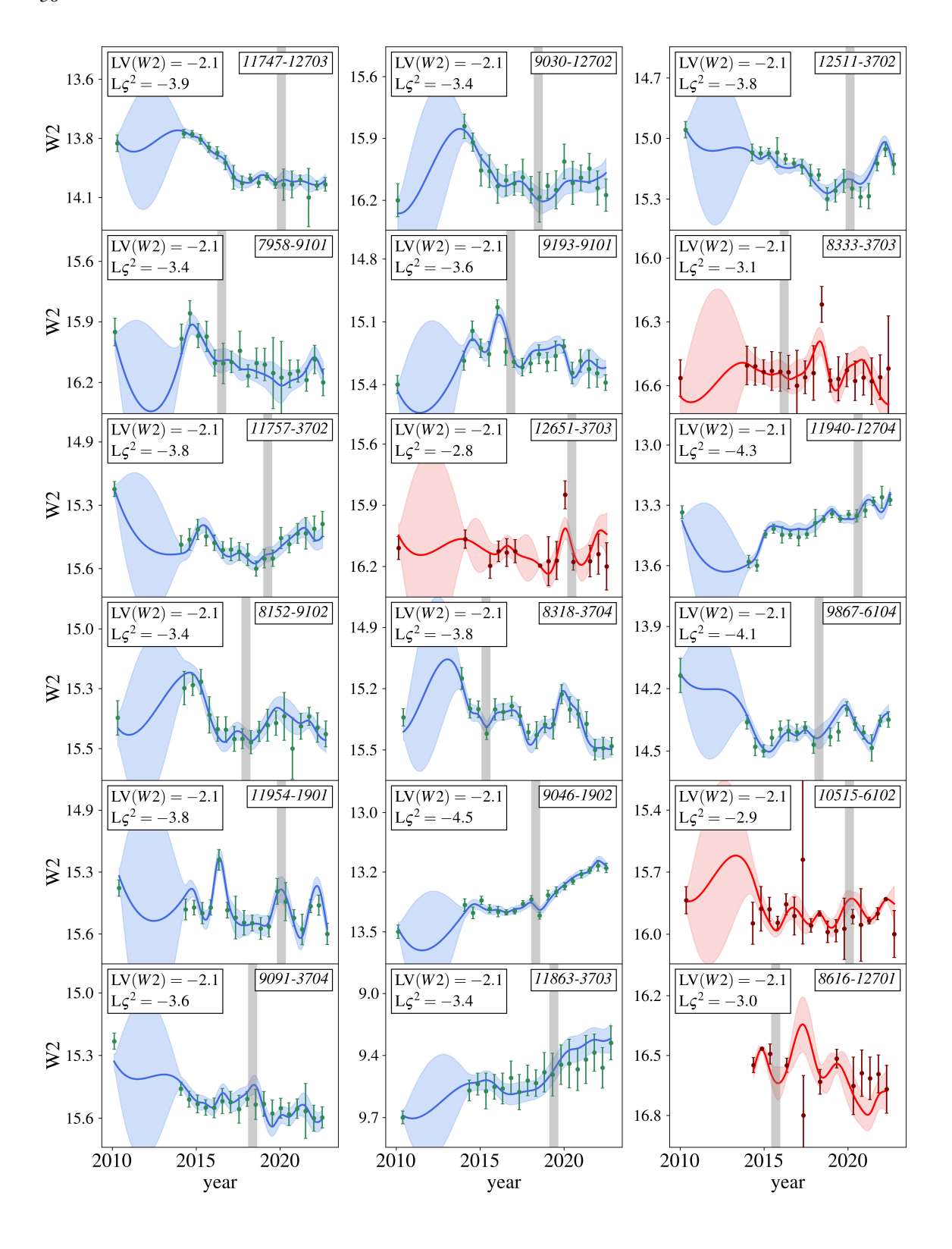


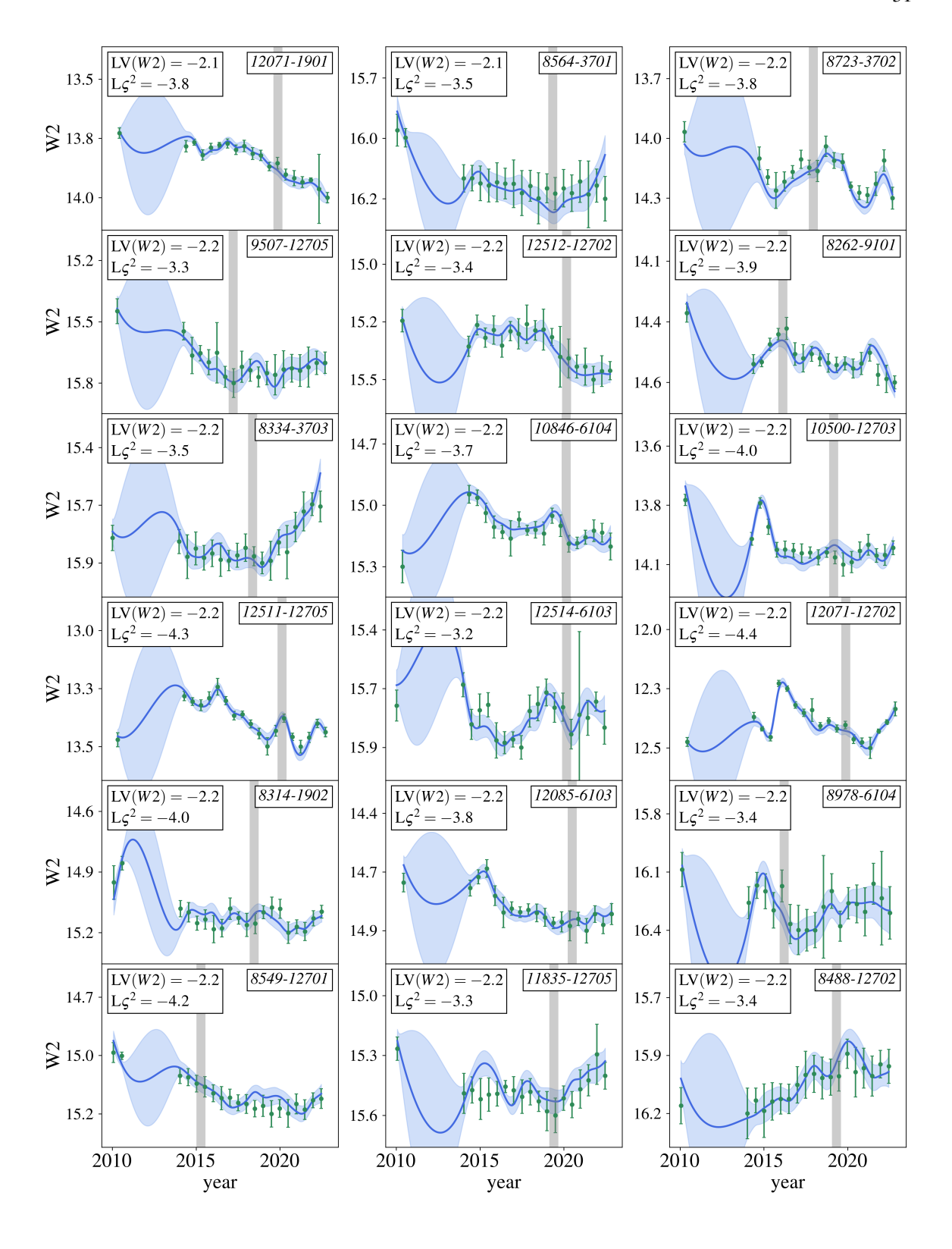


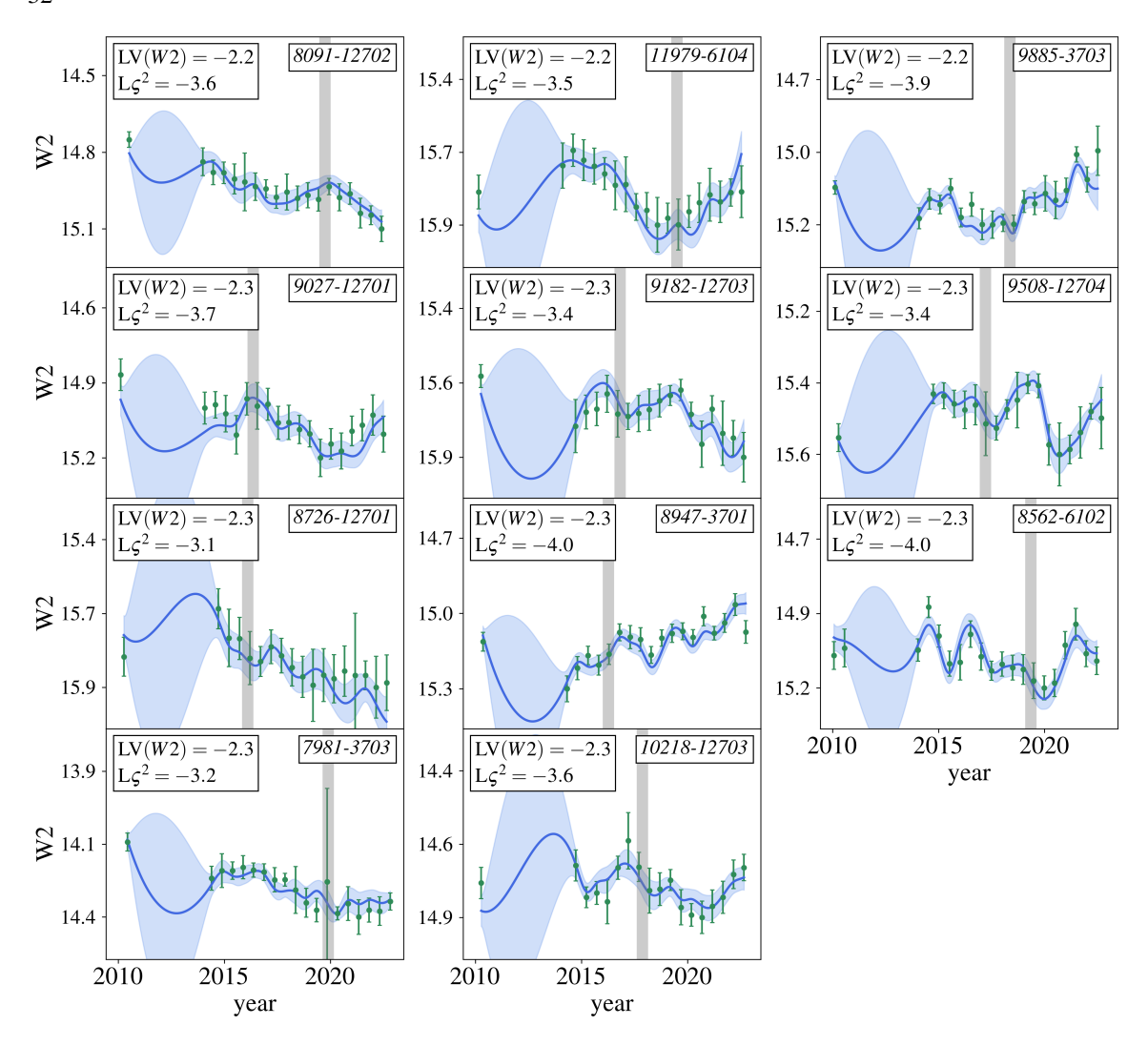












All Authors and Affiliations



¹Center for Cosmology and Particle Physics
Department of Physics, New York University, 726 Broadway, New York, NY 10003, USA
²Department of Physics and Astronomy, Siena College, 515 Loudon Road, Loudonville, NY 12211, USA